Appendix 2

Research Article | Vol. 27, No. 7 | 1 Apr 2019 | OPTICS EXPRESS 9361
Optics EXPRESS

Influence of coating technology and thermal annealing on the optical performance of AR coatings in iodine-filled absorption cells

JINDŘICH OULEHLA, PAVEL POKORNÝ, JAN HRABINA,* MIROSLAVA HOLÁ, ONDŘEJ ČÍP, AND JOSEF LAZAR

[1]*Institute of Scientific Instruments, Department of Coherent Optics, Czech Academy of Sciences, Královopolská 147, 61264 Brno, Czech Republic*
**hrabina@isibrno.cz*

Abstract: In this contribution, we investigate the properties of antireflective coatings on iodine-filled absorption cell windows. These coatings are subject to high temperatures during the cell production process and are in direct contact with the absorption medium, which influences their optical performance. We tested the thermal resistance of TiO_2- and Ta_2O_5-based coatings produced using conventional electron beam evaporation (e-beam) and ion-assisted deposition (PIAD). We prepared a set of iodine-filled absorption cells that were used to test the coatings' resistance to iodine vapors. We show that the choice of coating materials, coating methods, and a well-chosen bakeout procedure can mitigate any unwanted effects, such as temperature-induced spectral shifts and optical losses inhomogeneities or settling of the absorption medium in the coating.

1. Introduction

There are multiple deposition techniques of dielectric optical thin films. The most common are electron beam evaporation, plasma ion assisted deposition, magnetron sputtering or ion beam sputtering [1]. In this article we will deal with electron beam evaporation both conventional and plasma ion assisted. Conventional electron beam (e-beam) evaporation uses an electron beam to melt and evaporate the source material in a vacuum chamber. During deposition, the chamber pressure is low enough for the source material molecules to reach the substrate.

Plasma ion assisted deposition (PIAD) uses a plasma ion source in the vacuum chamber which directs a cone of plasma towards the substrates. The main difference from e-beam is a higher kinetic energy of the condensing material particles. Coatings prepared using this method have a higher refractive index and packing density than coatings prepared using e-beam only [2].

One of many applications of thin film coatings deposited on optical elements is in the area of absorption cells used as optical frequency references for frequency locking of lasers. The physical properties of the absorption medium and the optical properties of the cell itself determine the achievable parameters of the standard. The absorption cells are commonly developed in the form of bulky glass tubes, where the laser beam enters the inner volume through an optical window, interacts with the absorption medium inside the cell and leaves through an output optical window to a photodetector [3,4]. The most common absorbing media for stabilization of laser standards in present days are molecular iodine (mainly for visible spectral range) and acetylene (telecom wavelengths), because they offer the best spectral properties for laser locking [5–10]. Several absorption media (including iodine) are highly corrosive (especially for metallic materials) and sensitive to the presence of impurities and contaminants [3,4,11]. Moreover, especially in term of alkali vapors filled cells, problem of relaxation of excited atoms to ground state due to collisions with the cell walls caused

#355459 https://doi.org/10.1364/OE.27.009361
Journal © 2019 Received 14 Dec 2018; revised 8 Mar 2019; accepted 11 Mar 2019; published 18 Mar 2019

reduction of achievable frequency stabilities. Also in these cases, a special coatings of the cell walls can reduce these unwanted effects [12,13].

Modern approach to the design of optical frequency references includes utilization of hollow-core photonic crystal fibers, where the mass and volume of the reference is drastically reduced and the interaction lengths of the light beam and the medium can be extended to units/tens of meters [14–17]. The main factor limiting broader application of these fiber-based references can be seen in lower achievable frequency stability due to transit-time and collision broadening of the absorption lines.

Antireflection coatings deposited on the cell windows and optical fiber ends can significantly reduce optical losses, laser light back-reflections and unwanted resonator effects [18]. Especially in compact laser setups, the cells are often used in multi-pass arrangements [10,19]. In this case the inner surface of the windows can be coated with a combination of antireflection and high-reflective coatings to produce the multiple reflections of the beam through the medium. As the quality and spectral properties of the coatings affect the optical parameters of the reference, it has also a direct impact on the performance of the whole laser standard.

The optical windows can be attached to the cell body/tube by several techniques. One possibility is using special vacuum-compatible glue or solder. The windows can be also connected by optical contacting technique, where no additional material/chemical is needed. This technique needs demanding equipment for high precision polishing of optical surfaces, and it is more suitable for connecting optical elements with larger surfaces than the 1-2 mm wide joints between the cell tube and windows [19]. The third approach for connecting the optical windows to the cell body is the quartz welding method. The potential risk of thermal stress and degradation of the coatings caused by welding flame can be minimized by proper mechanical design of the windows [4]. The windows are in this case typically equipped with facets, so the thermal energy needed for melting of windows boundaries is reduced and transit of the heat to the coatings is minimized (Fig. 1).

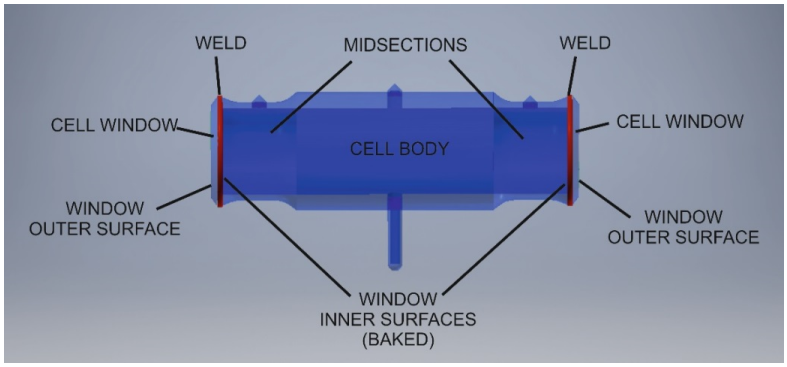

Fig. 1. Drawing of one half of the absorption cell with depicted welding areas and window outer and inner surfaces. A pair of windows is used for each cell. The window inner surface is AR coated before the welding process, the window outer surface is coated after. The inner surfaces of both the windows are baked out as they are the ones thermally influenced.

Depositing the coating on every active surface means that some of the coatings are in a direct contact with the medium inside the cell. Due to this fact, the material of the coating itself must also ensure non-reactivity and inertness to the absorption medium. Furthermore, the coatings have to be prepared in a way that avoids settling of the medium particles in the coatings structure.

Optics EXPRESS

In this article we investigate the influence of high temperatures and the presence of corrosive iodine vapors on the antireflective coatings properties and its dependence on coating materials and deposition technologies.

In the following investigation we especially concentrate on performance of antireflection coatings for 532 and 633 nm wavelengths, where molecular iodine-stabilized laser standards commonly operate. However, the general results are applicable for different coating designs and desired wavelengths as well.

2. AR coatings for 532 and 633 nm wavelengths

For our experiments we prepared four types of coatings deposited on four sets of fused silica substrates (FS). The aim of these experiments was to investigate the differences in coating materials and deposition techniques and their influence on sensitivity to thermal stress, and on the optical performance of the iodine absorption cells.

The fused silica substrates are 1" in diameter and 5 mm thick. One surface is polished to optical quality of λ/10, the other surface is fine ground to minimize back surface reflections.

When designing an antireflective coating there are several coating materials to choose from. In our case we wanted to investigate the materials we commonly use as they are relatively cheap, easy to work with and have a good optical performance. We chose TiO_2 and Ta_2O_5 as the high refractive index material and SiO_2 as the low refractive index material. The optical designs of the coatings are summarized in Table 1.

Table 1. Optical Coating Designs[a,b]

	TiO_2/SiO_2 PIAD	TiO_2/SiO_2 e- beam	Ta_2O_5/SiO_2 PIAD	Ta_2O_5/SiO_2 e-beam
	t [nm]	t [nm]	t [nm]	t [nm]
1H	22.3	25.9	27.2	25.7
2L	42.3	32.2	28.2	29.4
3H	43.4	60.5	77.3	76.6
4L	111.4	104.1	98.6	99.4

[a] t – Physical Thickness, H – High Refractive Index Material (TiO_2 or Ta_2O_5), L – Low Refractive Index Material (SiO_2), FS – Fused Silica Substrate.

[b] Numbers in the first column denote the individual layers starting from the substrate.

The coatings were produced using a SYRUSpro 710 coating system made by Bühler (formerly Leybold Optics). All coatings of one particular type were prepared in a single batch to ensure the same conditions for all samples. The deposition parameters can be found in Table 2. The substrate temperature was 300 °C in case of e-beam and approx. 260 °C in case of PIAD. The plasma source used was APSpro by Bühler.

Table 2. Deposition Parameters

		e-beam		PIAD		
Layer	**starting material**	**dep. rate**	**O_2 pressure**	**dep. Rate**	**O_2 flow**	**BIAS voltage**
SiO_2	Umicore SiO_2 granulate	1.5 nm/s	2.10^{-4} mbar	0.40 nm/s	5 sccm	145V
TiO_2	Umicore Ti_3O_5 tablets	0.5 nm/s	4.10^{-4} mbar	0.25 nm/s	23 sccm	110V
Ta_2O_5	Umicore Ta_2O_5 granulate	0.4 nm/s	4.10^{-4} mbar	0.20 nm/s	22 sccm	110V

The residual spectral reflectance characteristics measured by Varian Cary 5 spectrophotometer are in Fig. 2. All of the samples exhibit residual reflectance equal to or lower than 0.1% at the desired wavelengths (532/633 nm).

Optics EXPRESS

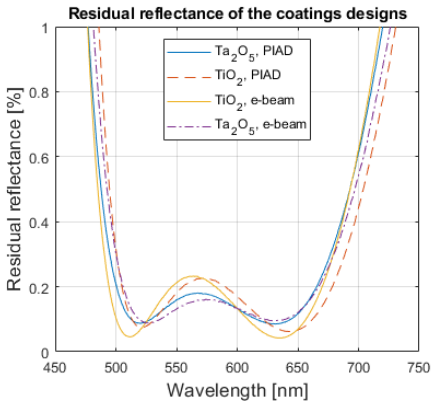

Fig. 2. Spectral profiles comparison of the TiO_2/SiO_2 and Ta_2O_5/SiO_2 coatings deposited by PIAD and e-beam techniques respectively.

3. Thermal resistance of dielectric coatings based on TiO_2 and Ta_2O_5 materials

The temperature influence on the coatings' optical properties (degradation, spectral shifts) were investigated by exposing the samples to various temperatures (350-1000°C) in a PID regulated electrical furnace. The applied temperature influence control loop steps include: 1/ heating up from room temperature to the desired temperature (heating rate 1000°C/1 hour), 2/ keeping the desired temperature for 2 hours, 3/ spontaneous cooling back to room temperature. For each bakeout procedure temperature level, new AR coated FS sample from the set was used. The residual reflection of tested substrates was evaluated by the spectrophotometer (Varian Cary 5). The thermally induced spectral shifts of all samples (e-beam TiO_2, e-beam Ta_2O_5, PIAD TiO_2, PIAD Ta_2O_5) are summarized in Fig. 3, detailed results from desired AR wavelengths (532 and 633 nm) are pointed out in Fig. 4.

The results show that PIAD coatings have a better resistance to high temperatures. They exhibit very low spectral shifts and perform reasonably well at both 532 nm and 633nm up to 1000 °C in case of TiO_2 and 900 °C in case of Ta_2O_5. The e-beam prepared coatings spectral performance fails at lower temperatures. The plasma ion assist transfers its kinetic energy to material particles, which are condensing on substrate [20]. E-beam coatings form a columnar structure, while PIAD coatings form a dense structure on the surface, which is less susceptible to thermal treatment [21]. The measurement also confirms that comparing to Ta_2O_5/SiO_2 coatings, where the thermally induced spectral shifts play a role in case of bakeout temperatures over ~600°C, TiO_2/SiO_2 coatings show better properties. The same ion energy was used for both TiO_2 and Ta_2O_5. As there is a difference in mass of these materials, they might be affected differently by the ion assist, which may result in a different microstructure and susceptibility to thermal treatment. The surface morphology of the samples was inspected by AFM (atomic force microscopy) and we did not observe any changes of the surface with the temperature.

It must be pointed out that the presented results of bakeout procedures were done for a relatively short exposure times (~2 hours) and slow thermal shock rate (1000°C/hour). The mid-term and long-term impacts are planned for investigation in future work together with dramatically faster cooling of the heated coatings. However, we did not observe any differences in the results of two hours and ten hours long bakeout procedures. Moreover, repeated measurement of the spectra after one month of the initial bakeout procedure did not show any spectral changes during this period. We also expect that the thermal expansion coefficient of used substrate material (fused silica) is small enough to prevent the coatings against thermal shock induced mechanical cracking (discussed below in section 4).

Optics EXPRESS

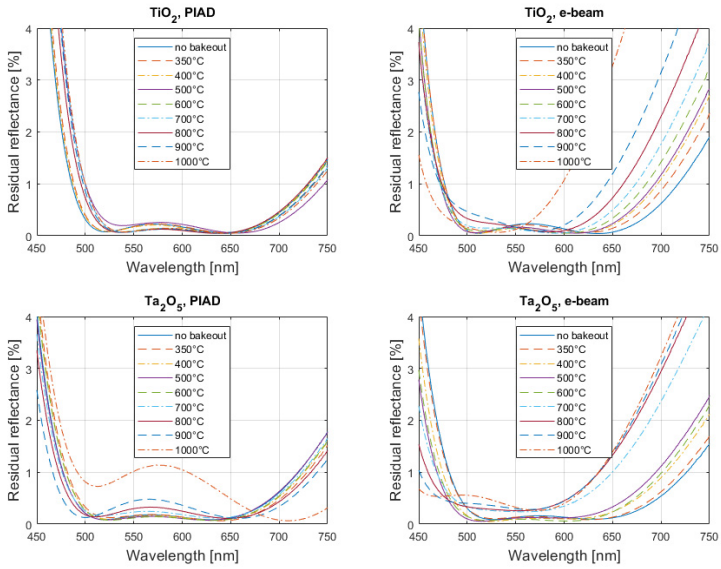

Fig. 3. Bakeout procedure induced spectral shifts of the antireflection coatings deposited by different methods (e-beam/PIAD) and using TiO_2,Ta_2O_5 as high refractive index materials – overall visible spectral range.

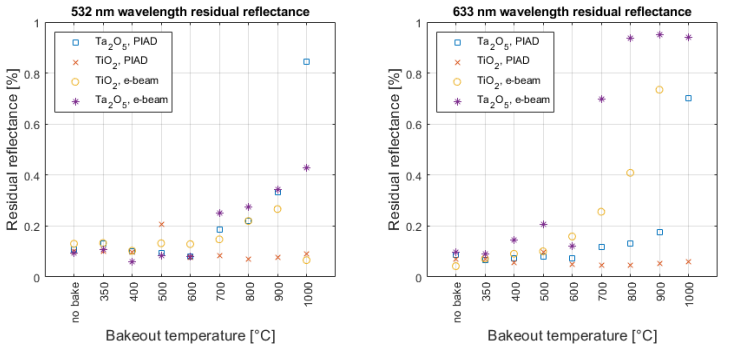

Fig. 4. Bakeout procedure induced spectral shifts of the antireflection coatings deposited by different methods (e-beam/PIAD) and using TiO_2,Ta_2O_5 as high refractive index materials – details on desired AR coating wavelengths 532 and 633 nm. Red crosses: TiO_2/PIAD, yellow circles: TiO_2/e-beam, purple stars: Ta_2O_5/e-beam, blue squares: Ta_2O_5/PIAD.

4. Spectral and optical properties of baked out AR coatings for iodine absorption cells windows

Considering the results from comparison between TiO_2 and Ta_2O_5 coatings material in section 3, we decided to use TiO_2/SiO_2 material combination and PIAD deposition method for testing its suitability for AR coatings for iodine absorption cells windows. The design of the coatings was the same as in bakeout procedure test described in section 3. The cells set consisted of 6 cells filled with ultra-pure molecular iodine $^{127}I_2$. The whole cells (including optical windows) were made of fused silica material, the windows were equipped with safety facets and were

joined to the cell body midsections by quartz welding. The active length was 200 mm and active diameter of the windows (AR coatings diameter) was 22 mm.

4.1. AR coatings spectral properties in context of iodine absorption cells technology steps

The cell windows inner surfaces were AR coated, then the windows were baked out. After baking out, the windows were welded onto the midsection and then their outside surfaces were AR coated. The evaluation of the coatings spectral properties after each individual cell manufacturing technology step consists of: 1/ residual reflectance measurement of the window surfaces after the welding of the window to midsections of the cell body, 2/ transmittance measurement through the cell after welding all of its parts together (midsections with windows welded to central part), 3/ transmittance measurement after the filling of the cell with the iodine media.

Considering the results of thermal resistance presented in section 3, we decided to apply the bakeout procedures as follows: PIAD-no bakeout, 800°C, 900°C and e-beam-no bakeout, 600°C, 800°C. The baked windows with connected midsection parts were then coated from outer sides and residual reflectance of both sides of the windows were evaluated by the optical spectrophotometer Agilent Cary 7000. The diagrams in Fig. 5 present means of averaged residual reflectance measured from pairs of windows tested from inner and also outer sides.

Investigation of the results found that the baking procedure did not cause significant spectral profiles changes, the residual reflectance at desired wavelengths still stays below 0.25% for all baking temperature cases. The main difference can be observed in the graph PIAD / 900°C with spectral red shift of ~10 nm.

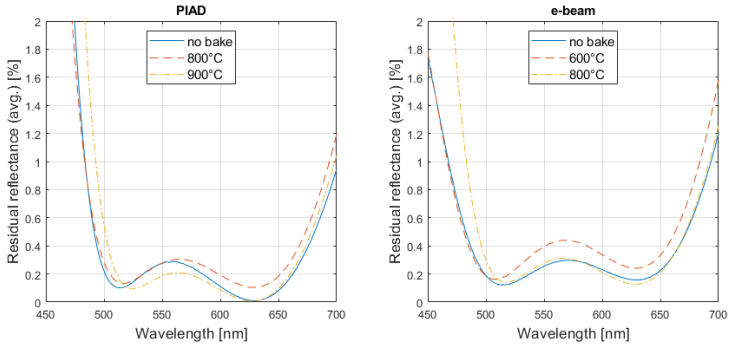

Fig. 5. Residual reflectance of the deposited windows (inner coatings baked out), averaged over the pair of windows and inner/outer surface measurement.

The finished windows with midsections were than welded to the central parts of the cells, the cells were completed and prepared for filling with iodine. The transmittance of the completed cells (before filling) is shown in Fig. 6. The size of the spectrophotometer sample compartment allows for placing of the whole cell to the path of the focused light beam, with the optical waist in the middle of the cell length. Because of the length of the cells (~200 mm) and the divergence of the beam, the cross section of the beam at the windows positions is ~15x15 mm and covers almost the whole surface of the coatings.

Optics EXPRESS

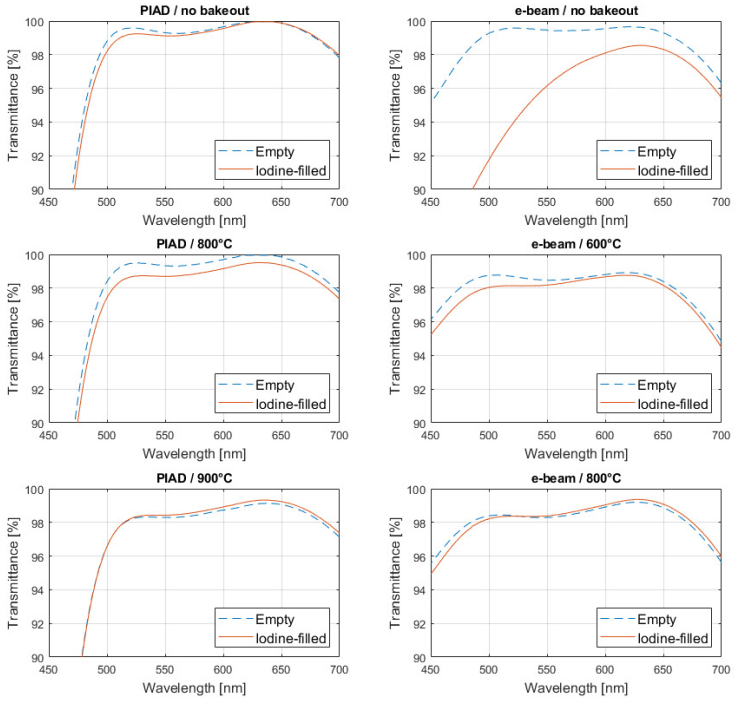

Fig. 6. Transmittance through the whole cells before their filling with iodine absorption media (blue lines) and after their filling with iodine absorption media (red lines). The iodine molecules were stored in liquid nitrogen trap.

The investigation of the final transmittance through the cells was done after the filling of the cells with iodine media using the same optical arrangement in the spectrophotometer as in the previous step. To avoid the optical absorption caused by the iodine vapor, the cold finger of the cell was placed in liquid nitrogen (LN_2) trap where the iodine was stored in a solid state. After several tens of minutes of LN_2 cooling, the transmittance spectra were recorded.

The transmission measurement results in Fig. 6 confirm the thermally induced effects in the spectral properties of the coatings. In case of the PIAD method, the bakeout procedure of up to 800°C level causes negligible changes (losses ~0.1% per coating) of optical transmittance at desired wavelengths. With the thermal stress induced by bakeout temperature of 900°C, the losses increase to levels of 0.6% (532 nm) and 0.3% (633 nm) per coating respectively. In comparison to these results, the coatings deposited by conventional e-beam method exhibit much higher sensitivity to applied bakeout temperatures, optical losses reach 0.5% (532 nm) and 0.3% (633 nm) per coating for 600°C and 0.65% (532 nm) and 0.25% (633 nm) per coating for 800°C bakeout temperature levels.

Moreover, in comparison to conventional e-beam technology, the use of the PIAD method in optical coatings deposition dramatically reduces the sensitivity of the coatings to the settling of the iodine molecules in the coating structure (Fig. 6). The results also confirm that this unwanted effect in e-beam deposition can be mostly suppressed by proper coatings

bakeout before filling the cell with the iodine media (but finding an acceptable compromise against deformation of the spectra caused by baking out is necessary).

4.2. Optical losses homogeneity of the cells' windows AR coatings

Considering the limitations of spectrophotometer spot size of ~15 x 15 mm, we decided to map the AR coatings' optical losses homogeneity at λ = 532 nm using laser beam. The filled cells were put into simple optical system consisted of frequency doubled Nd:YAG laser and a photodetector unit. The frequency of the laser was detuned far away from any visible iodine absorption line in the cell and further the iodine in the cell under the test was trapped in liquid nitrogen (LN_2) trap. In this arrangement we were able to monitor optical losses on the cell windows (4 interfaces in total) by the optical power meter. Thanks to small diameter size of the laser beam (~1 mm) we were able to monitor these losses in different areas of the windows. The correctness of this method has been verified by comparison of the transmittance measurement of the iodine filled cell (solid iodine trapped by LN_2 trap) and measurement of reopened and washed cell. The washing procedure included slight heating of the cell windows with the hot-air gun (~60°C) with simultaneous rinse of the argon gas for helping the iodine to get off the inner volume of the cell. The washing was applied for 30 minutes. The resulting transmittance, which was ~0.2% lower after the washing than in case of the iodine filled cell (due to absorption caused by residual iodine settling on AR coatings) confirms that using of LN_2 trap in our measurements is a reliable method for keeping the iodine out of the coatings.

The results of total optical losses measured through both cell windows (1 beam pass) at 9 different positions (1 in center, 4 between center and periphery and 4 in the coating periphery) for each of the cells are plotted in Fig. 7.

Considering the estimated accuracy of the laser measurement (± 0.1%), the results show the same trends as with previously obtained data from the spectrophotometry measurement. The use of the ion assist (PIAD) in the coating formation significantly contributes to better thermal resistance of the coating. According to the results of the tested coatings, there is a minimal impact of spectral shifts or degradation of the coatings to resulting optical losses for bakeout temperatures for up to at least 800 °C. The standard deviations of the homogeneity of the optical losses at different window locations are well below 0.5% (averaged per 4 coatings interfaces).

Regarding the coatings produced without ion assist, there is an evident impact of the iodine absorption medium to the resulting optical losses. The iodine molecules probably settle and are trapped in the porous structure of the coatings and cause additional light absorption. The worst case (the windows deposited with coating without ion assist and without bakeout procedure) exhibit very high losses at levels up to 6% per pass through the cell. When we consider that this unwanted iodine settling effect acts only on the inner surfaces of the cell and the outer losses per coating is at or below 0.2% level, we obtain the losses at least at 2.8% per one coating-iodine interface.

However, the bakeout procedure can significantly reduce this effect, as shown by results from "e-beam / 600°C" and "e-beam / 800°C" diagrams in Fig. 7. Considering the coating design under the test and minding the results from above presented measurements, one can find a suitable compromise between bakeout temperature level (spectral shift and degradation of the coating) and the level of iodine settling effect between 600 and 800°C. Furthermore, thermal impact on the coating structure is confirmed by the inhomogeneity of optical losses of the "e-beam – no bakeout" cell. The standard deviation of the losses at different location of the windows is at 1.5% level, at least three times higher than in case of the PIAD deposited cells. Moreover, in general this cell exhibits lower level of losses close to the coating edge, caused by the glasswork burner induced thermal stress around the edges during the welding of the windows. This result confirms heat influence on the coatings-iodine reactivity/settling effect.

Optics EXPRESS

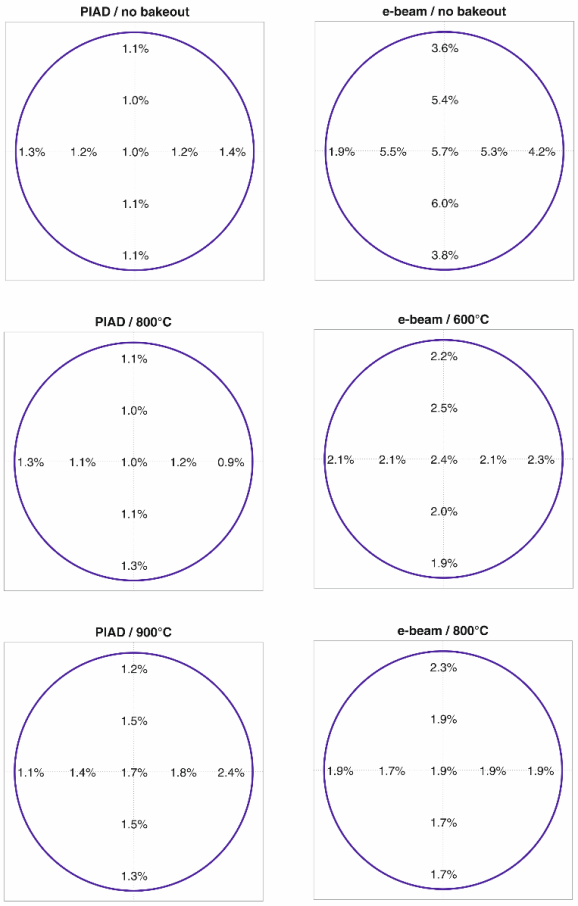

Fig. 7. Measurement of the coatings optical losses homogeneity at different windows locations (total optical losses at 532 nm wavelength over 1 cell pass = 4 interfaces coatings/environment).

4.3. Evaluation of the iodine purity

One of the potential reasons for degradation of the coatings optical properties can be found in contamination with the iodine and formation of unwanted iodine based compounds settling down/reacting with the windows coatings. The evaluation of the chemical purity and non-reactivity of the iodine media against materials of the coatings was realized through the laser induced fluorescence method (LIF), well described in [3,4,22]. This technique is based on measurement of dependency between the relative level of induced fluorescence on iodine pressure, expressed by Stern-Volmer formula [22] and resulted in Stern-Volmer coefficient (K [Pa]) describing the purity level. The cells are rated as: excellent (K<1 Pa), good (K between 1 and 1.5 Pa) and contaminated (K>1.5 Pa). All of the iodine cells were tested by the LIF system and they show excellent purity with the Stern-Volmer coeficient (K) at 0.76-0.93 Pa level (Table 3).

Table 3. Stern-Volmer Coefficients of the Tested Iodine Cells

Cell name	Stern-Volmer coefficient K [Pa]
PIAD / no bakeout	0.91
PIAD / 800°C	0.84
PIAD / 900°C	0.76
e-beam / no bakeout	0.76
e-beam / 600°C	0.83
e-beam / 800°C	0.93

These results confirm the high-level purity of iodine medium in the cells and there is no chemical reaction of iodine with the coatings materials. This evaluation also confirms that the high level of optical losses found in the measurement (especially the cell "e-beam / no bakeout") is caused by the settling of iodine molecules in the structure of the coating surface. This effect can be reduced by using of the PIAD and proper bakeout procedure of the coatings before the filling of the cell with the iodine.

5. Conclusions

This work was oriented towards the influence of thermal annealing to spectral properties of dielectric optical coatings on iodine absorption cells windows. Two different coating material combinations (TiO_2/SiO_2 and Ta_2O_5/SiO_2) and two different deposition methods (conventional e-beam and plasma ion assisted deposition) were studied from the point of view of antireflective coatings' resistance to applied bakeout temperatures and chemically aggressive environment.

TiO_2 based PIAD coating is the most resistant against temperature induced spectral shifts. Temperatures up to 1000°C do not produce any significant shifts in the spectrum and the coating performs well at both 532 nm and 633 nm wavelengths. In case of both TiO_2 and Ta_2O_5, PIAD coatings show better thermal resistance than conventional e-beam.

In terms of iodine-filled absorption cells, the proper bakeout procedure can significantly reduce optical losses of the AR coatings due to the iodine settling into the coating. In case of TiO_2 based PIAD coating baked to 900°C we achieved optical losses at the inner surface of 0.3% level, while in case of e-beam based coating without bakeout procedure this losses dramatically increased up to 2.8% level per inner surface.

The resulting spectral characteristics confirm that by selection of proper deposition method and optimized bakeout temperature, the unwanted effect of settling of the iodine in the coating structure can be effectively suppressed and the performance of laser standards based on these iodine cells can be further improved.

Funding

Grant Agency of the Czech Republic (GA15-18430S); Ministry of Education, Youth and Sports of the Czech Republic (LO1212); Ministry of Education, Youth and Sports of the Czech Republic and European Commission (CZ.1.05, 2.1.00, 01.0017); Czech Academy of Sciences (RVO: 68081731, Strategy AV21).

Acknowledgments

The authors wish to express thanks to Tatiana Šarlejová and Stanislav Šlechtický for their development of tested iodine absorption cells and preparation of the optical elements used in this research work.

References

1. H. A. Macleod, "Recent developments in deposition techniques for optical thin films and coatings," in *Optical Thin Films and Coatings - From Materials to Applications*, A. Piegari and F. Flory, eds. (Woodhead Publishing Limited, 2013), pp. 3–25.
2. G. Atanassov, J. Turlo, J. K. Fu, and Y. S. Dai, "Mechanical, optical and structural properties of TiO2 and MgF2 thin films deposited by plasma ion assisted deposition," Thin Solid Films **342**(1-2), 83–92 (1999).

Optics EXPRESS

3. M. Zucco, L. Robertsson, and J. P. Wallerand, "Laser-induced fluorescence as a tool to verify the reproducibility of iodine-based laser standards: a study of 96 iodine cells," Metrologia **50**(4), 402–408 (2013).
4. J. Hrabina, M. Zucco, C. Philippe, T. M. Pham, M. Holá, O. Acef, J. Lazar, and O. Číp, "Iodine absorption cells purity testing," Sensors (Basel) **17**(1), 102–114 (2017).
5. J. Lazar, J. Hrabina, P. Jedlicka, and O. Cip, "Absolute frequency shifts of iodine cells for laser stabilization," Metrologia **46**(5), 450–456 (2009).
6. G. D. Rovera, F. Ducos, J. J. Zondy, O. Acef, J. P. Wallerand, J. C. Knight, and P. S. Russell, "Absolute frequency measurement of an I-2 stabilized Nd: YAG optical frequency standard," Meas. Sci. Technol. **13**(6), 918–922 (2002).
7. R. Holzwarth, A. Y. Nevsky, M. Zimmermann, T. Udem, T. W. Hansch, J. Von Zanthier, H. Walther, J. C. Knight, W. J. Wadsworth, P. S. J. Russell, M. N. Skvortsov, and S. N. Bagayev, "Absolute frequency measurement of iodine lines with a femtosecond optical synthesizer," Appl. Phys. B **73**(3), 269–271 (2001).
8. P. Balling, M. Fischer, P. Kubina, and R. Holzwarth, "Absolute frequency measurement of wavelength standard at 1542nm: acetylene stabilized DFB laser," Opt. Express **13**(23), 9196–9201 (2005).
9. J. Hald, L. Nielsen, J. C. Petersen, P. Varming, and J. E. Pedersen, "Fiber laser optical frequency standard at 1.54 μm," Opt. Express **19**(3), 2052–2063 (2011).
10. C. Philippe, R. Le Targat, D. Holleville, M. Lours, T. Minh-Pham, J. Hrabina, F. Du Burck, P. Wolf, and O. Acef, "Frequency tripled 1.5 μm telecom laser diode stabilized to iodine hyperfine line in the 10-15 range," Eur. Freq. Time Forum **1**, 7477827 (2016).
11. J. Hrabina, M. Šarbort, O. Acef, F. D. Burck, N. Chiodo, M. Holá, O. Číp, and J. Lazar, "Spectral properties of molecular iodine in absorption cells filled to specified saturation pressure," Appl. Opt. **53**(31), 7435–7441 (2014).
12. R. Straessle, M. Pellaton, C. Affolderbach, Y. Petremand, D. Briand, G. Mileti, and N. F. de Rooij, "Microfabricated alkali vapor cell with anti-relaxation wall coating," Appl. Phys. Lett. **105**(4), 043502 (2014).
13. W. H. Li, M. Balabas, X. Peng, S. Pustelny, A. Wickenbrock, H. Guo, and D. Budker, "Characterization of high-temperature performance of cesium vapor cells with anti-relaxation coating," J. Appl. Phys. **121**(6), 063104 (2017).
14. A. Lurie, P. S. Light, J. Anstie, T. M. Stace, P. C. Abbott, F. Benabid, and A. N. Luiten, "Saturation spectroscopy of iodine in hollow-core optical fiber," Opt. Express **20**(11), 11906–11917 (2012).
15. P. T. Marty, J. Morel, and T. Feurer, "All-fiber multi-purpose gas cells and their applications in spectroscopy," J. Lightwave Technol. **28**(8), 1236–1240 (2010).
16. M. Triches, M. Michieletto, J. Hald, J. K. Lyngsø, J. Lægsgaard, and O. Bang, "Optical frequency standard using acetylene-filled hollow-core photonic crystal fibers," Opt. Express **23**(9), 11227–11241 (2015).
17. T. Talvard, P. G. Westergaard, M. V. DePalatis, N. F. Mortensen, M. Drewsen, B. Gøth, and J. Hald, "Enhancement of the performance of a fiber-based frequency comb by referencing to an acetylene-stabilized fiber laser," Opt. Express **25**(3), 2259–2269 (2017).
18. J. Seppa, M. Merimaa, A. Manninen, M. Triches, J. Hald, and A. Lassila, "Interference cancellation for hollow-core fiber reference cells," IEEE Trans. Instrum. Meas. **64**, 1595–1599 (2015).
19. T. Schuldt, K. Doringshoff, A. Milke, J. Sanjuan, M. Gohlke, E. V. Kovalchuk, N. Gurlebeck, A. Peters, and C. Braxmaier, "High-performance optical frequency references for space," J. Phys.: Conf. Ser. **723**, 012047 (2016).
20. M. S. Farhan, E. Zalnezhad, and A. R. Bushroa, "Properties of Ta2O5 thin films prepared by ion-assisted deposition," Mater. Res. Bull. **48**(10), 4206–4209 (2013).
21. S. H. Woo, C. K. Hwangbo, Y. B. Son, I. C. Moon, and G. M. Kang, "Optical properties of Ta2O5 thin films deposited by plasma ion-assisted deposition," J. Korean Phys. Soc. **46**, S187–S191 (2005).
22. S. Fredin-Picard, "A study of contamination in I-127(2) cells using laser-induced fluorescence," Metrologia **26**(4), 235–244 (1989).

Appendix 3

Compact interferometric displacement gauge with sub-nanometer resolution and milimeter range

Simon Rerucha, Miroslava Hola, Martin Sarbort, Jindrich Oulehla, Bretislav Mikel, Josef Lazar and Ondrej Cip
ISI - Institute of Scientific Instruments of the CAS, v.v.i
Kralovopolska 147, 61264 Brno, Czech Republic
Email: res@isibrno.cz (S. R.)

***Abstract*—We report on the design and prototype realization of the gauge probe sensor for the measurement of displacement based on a laser interferometer. The measurement system incorporates a suitable laser source and interferometric phase processing system. The phase extraction (fringe counting) relies on a single-detector homodyne detection method for phase extraction that uses a harmonic optical frequency modulation of the laser beam and allows for a significantly reduced and thus compact and robust optical arrangement. The experimental verification revealed that the sensor system achieves the sub-nanometer precision and nanometer accuracy in the 10 mm measurement range.**

I. Introduction

The laser interferometry techniques represent the most precise methods for dimensional measurement with both the sub-nanometer precision and the large measurement range as well as ultimate accuracy, precision and repeatability [1]. The basic resolution of the laser interferometer corresponds to the wavelength of the laser source, usually to one half or one quarter of it, depending on the optical configuration. This resolution is typically improved by various methods, commonly referred to as fringe counting/subdivision or detection techniques [2], [3], that provide the resolution down to picometer range. Another advantage is that the inherently optical method allows for the traceability transfer into the mechanical domain.

One of the still relevant challenges is the application of its ultimate dynamic range (theoretically an infinite) and precision into practical instrumentation suitable e.g. for the mechanical engineering industry. Such an application, besides the obvious advantages introduces several issues that needs to be tackled: both the interferometers and the laser source require stable operation conditions, the optical setups tend to be mechanically fragile, bulky and expensive and that the routine long-term operation requires skilled maintenance.

In this paper we present a compact form-factor displacement gauging probe sensor for contact measurement based on a laser interferometer with a simplified optical arrangement. The pencil-type construction, similar to that of the LVDT sensors, features linearly guided contact tip with the 30 mm travel range, the housing from low-expansion material and adjustable mounts for the interferometer's optical components.

The research was supported by GA CR (GB14-36681G), TA CR (TA03010663, TA03010835, TA02010711, TE01020233), MEYS CR (LO1212), its infrastructure by MEYS CR and EC (CZ.1.05/2.1.00/01.0017) and by ASCR (RVO:68081731).

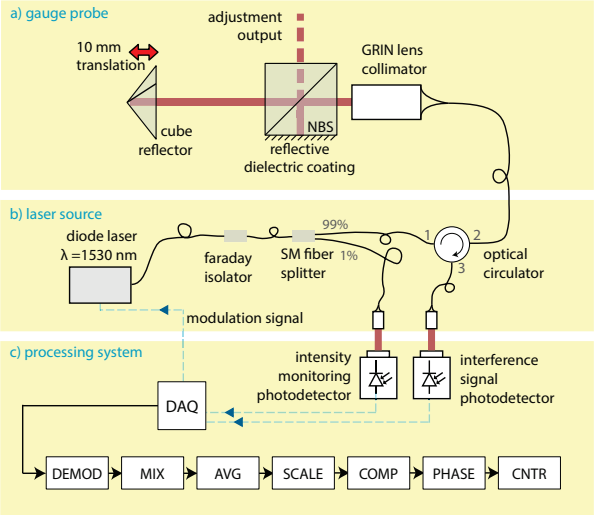

Fig. 1. The sensor system architecture: (a) the simplified optical arrangement of the interferometer fed from (b) the laser source. The (c) processing system acquires and processes the interferometer's output.

The interferometer, operating at 1.5 μm wavelength band, uses the Michelson's arrangement with our custom single-detector homodyne detection based on harmonic modulation of the laser wavelength. Sections II and III present the design and prototype realization of the sensor itself, an appropriate laser source for the embedded interferometer and the methods for the processing of the signal from the interferometer. Sections IV and V presents the experimental verification of the sensor performance.

II. Sensor Design

The entire sensor system incorporates several components: the measurement sensor itself (the gauge probe), the laser source and the processing subsystem. The body of the gauge probe basically provides the housing for the measuring tip and for the optical components of the laser interferometer. The processing system generates control signals for the laser and performs the fringe counting. The individual parts, shown in Fig. 1, are described in following sections.

978-1-4799-8287-5/16/$31.00 ©2016 IEEE

A. Optical Setup

The laser interferometer uses the Michelson interferometer arrangement (Fig. 1a) that uses a non-polarizing beam-splitter (NBS) cube to split the fiber-fed beam into the reference and measuring arm. The reference arm uses a flat mirror that is realized as a dielectric reflective coating deposited onto the wall of the NBS. The measurement uses a cube-corner reflector that is mounted on the translation mechanism of the measuring tip. As both the mirror coating in the reference arm and the reflector in the measuring arm reflect the beam in parallel to the incident beam and without a lateral offset so that the output of the interferometer is collected back by the collimator and fed to the processing subsystem. The laser delivery as well as the optical arrangement use a non-polarizing optics and single mode fibers.

B. Laser Source

As the laser source we used a compact laser-diode based module with integrated circuitry for the stabilization of the diode temperature and injection current. As the wavelength is longer in comparison to that of the He-Ne laser sources (traditionally used for dimensional metrology), the fundamental resolution is proportionally lower. On the other hand the fiber and optical components for the telecommunication wavelength band are significantly more abundant and thus cost-effective.

The laser output (see 1b), already fiber-coupled within the module, is passed through an Optical Faraday Isolator and to a single-mode fiber splitter. Small part of the light is sensed by a photodetector so that the processing system can monitor the intensity of the laser module output and compensate it's intensity fluctuations caused e.g. by the residual amplitude modulation that occurs as a consequence of laser frequency optical modulation. The rest of the light passes to the optical circulator that directs the beam from laser to the gauge probe and then directs the interferometer's output – that is transmitted back through the same fiber – to the interference signal photodetector.

C. Processing System

The processing subsystem carries out the fringe counting using a homodyne-based single-photodetector detection system, that relies on a harmonic modulation of the laser source optical frequency in order to reconstruct a pair of sine/cosine signals by means of numeric computation [4]. The calculations (see 1c) are done in the digital domain from digitized input analog signals from the photodetectors. First step is the synchronous demodulation (DEMOD) of the modulation effects caused by the optical frequency modulation of the laser. The demodulated part is mixed (MIX) with a phase shifted copy of the modulation signal. Then the signal is averaged (AVG) and scaled (SCALE) to produce the sine and cosine signals. Onto those the compensation of the residual amplitude modulation (that is caused by the optical frequency modulation) and scale linearity correction algorithms are applied (COMP; [4], [5]). The phase is then extracted (PHASE) and the displacement is calculated (CNTR).

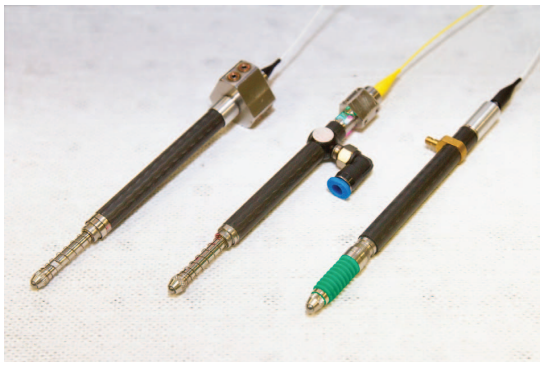

Fig. 2. Sensor prototypes (gauges only).

III. Prototype Fabrication

We have completed several sensor prototypes – shown in Fig. 2 – in order to carry out the experimental verification. The body of the sensor is fabricated from carbon fiber reinforced polymer that exhibits very low thermal expansion while it ensures rigid support for the rest of the mechanics. A commercially available measuring tip with a precise linear ball bearing was adjusted so that it can hold the retroreflector that acts as the measuring arm of the interferometer. The measuring tip is spring-expanded and air-retracted. An aluminum housing was fabricated to hold the $5\,\mathrm{mm}$ beam-splitter cube and the fiber collimator with the gradient-index lens. The position of the retroreflector and the beam splitter is factory adjusted while the collimator is adjustable in six degrees of freedom.

The laser module we use (RIO Orion Module by Redfern Integrated Optics) is lasing at the nominal wavelength of $1530.245\,\mathrm{nm}$. The module with the nominal output power of $10\,\mathrm{mW}$ and the line width $> 2\,\mathrm{kHz}$ is modulated with a sine signal with $50\,\mathrm{kHz}$ frequency and $\approx 150\,\mathrm{MHz}$ peak-to-peak modulation depth of the optical frequency.

The DAQ (Agilent U2531A) acquires the signals from the photodetectors at $400\,\mathrm{kSps}$ with $14-$bit resolution. The acquired data are transferred to a PC where a dedicated control software processes them in real-time (with a certain transport delay). The fundamental bandwidth of the displacement measurement is equal to the modulation bandwidth, i.e. with the single-pass arrangement the resulting maximum translation velocity reaches $\approx 9.5\,\mathrm{mm.s}^{-1}$. For measurements within the range $< \lambda/4$, the detection technique provides theoretical limit that is equal to the analog-to-digital sampling rate.

IV. Experimental Verification

We carried out two sets of experiment to verify the performance of the displacement sensor. In first set of experiment, we have assembled conventional Michelson interferometer with similar optical arrangement to that in the sensor and with two separate detection chains. The reference chain realized the four-detector homodyne detection while the other realized the tested method. On this setup we compared the coincidence of

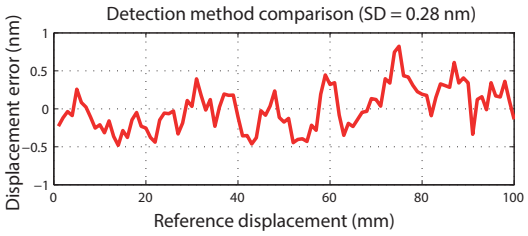

Fig. 3. The comparison of the single-detector phase detection technique against the reference detection method. The plot shows the difference between the reference displacement and displacement measured by the verified method.

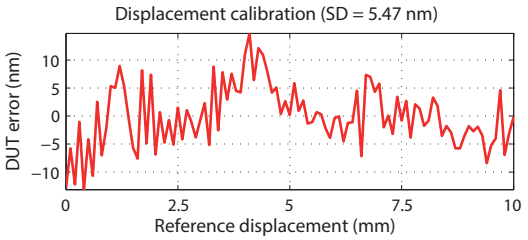

Fig. 4. Calibration results of the sensor prototype (referred to as DUT - Device Under Test), measured on the nano-calibrator.

the phase extraction between the two in order to separately verify the fringe counting method. The results of comparison on the 100 mm travel range are shown in Fig. 3.

The overall performance was inspected on a dedicated nano-comparator machine (developed at ISI[6]) which was constructed for the calibration of precise displacement sensors. The results, shown in Fig. 4, indicate the $\sigma = 5.5\,\mu$m accuracy over the 10 mm lift of the gauge probe.

V. Results and Discussion

The experimentation has revealed that the single-detector fringe counting technique used in conjunction with the interferomer operated with the $1.5\,\mu$m laser achieves better coincidence than $\lambda/1000$ in comparison to the traditional homodyne detection technique. The substantial benefit of the novel detection scheme is that it allows the use of non-polarization optics and single mode fiber for beam delivery. This combination also makes the system robust against the inevitable rotation of the polarization induced by the vibrations and movements of the delivery fiber. The drawback is the requirement for the optical frequency modulation capability in the laser source, which can be fortunately easily met with modern semiconductor laser sources.

The calibration measurement revealed that the displacement measurement error keeps below 10 nm. A benefit of the interferometric measurement is the feasibility of the traceability transfer from the optical domain to the mechanical domain, e.g. by the means of external stabilization of the laser source on an atomic transition in acetylene. Since the laser sources at the $1.5\,\mu$m are able to deliver high optical power (compared e.g. to stabilized He-Ne lasers) a single laser source could be used for driving multiple sensors in a complex measurement system. The system could also provide multiple-sensor applications referenced to a single scale (represented by the laser frequency), optionally including the traceability to a fundamental standard.

Please note that as the only interface between the gauge probe and the rest of the system is the optical fiber, the sensor system is immune to the EMI noise.

VI. Conclusion

We have developed the compact gauge probe sensor system that uses the principle of the laser interferometry for the precise displacement measurement. The use of the modulation-based interference phase detection method allowed for the construction of an interferometer with a significantly simplified optical arrangement so that the presented design integrates the ultimate precision of the laser interferometer with the endurance necessary for the manufacturing industry. The sensor system is feasible e.g. for multi-axis dimensional systems or for various length metrology applications.

References

[1] A. J. Fleming, "A review of nanometer resolution position sensors: operation and performance," *Sensors and Actuators A: Physical*, vol. 190, pp. 106–126, 2013.

[2] K. Birch, "Optical fringe subdivision with nanometric accuracy," *Precision Engineering*, vol. 12, no. 4, pp. 195–198, 1990.

[3] P. Hariharan, "Optical interferometry," *Reports on Progress in Physics*, vol. 54, no. 3, pp. 339–&, 1991.

[4] S. Rerucha, Z. Buchta, M. Sarbort, J. Lazar, and O. Cip, "Detection of Interference Phase by Digital Computation of Quadrature Signals in Homodyne Laser Interferometry," *Sensors*, vol. 12, no. 10, pp. 14 095–14 112, 2012.

[5] O. Cip and F. Petru, "A scale-linearization method for precise laser interferometry," *Measurement Science & Technology*, vol. 11, no. 2, pp. 133–141, 2000.

[6] M. Cizek, Z. Buchta, B. Mikel, J. Lazar, and O. Cip, "Interferometric nanocomparator for calibrating precision displacement sensors," ser. Proc. SPIE, vol. 7791, 2010, pp. 77 910N–77 910N.

Appendix 4

UŽITNÝ VZOR

(11) Číslo dokumentu:
33 046
(13) Druh dokumentu: **U1**
(51) Int. Cl.:
G01B 9/02 (2006.01)

(19) ČESKÁ REPUBLIKA

ÚŘAD PRŮMYSLOVÉHO VLASTNICTVÍ

(21) Číslo přihlášky: **2019-36255**
(22) Přihlášeno: **31.05.2019**
(47) Zapsáno: **30.07.2019**

(73) Majitel:
Ústav přístrojové techniky AV ČR, v.v.i., Brno, Královo Pole, CZ

(72) Původce:
Mgr. Šimon Řeřucha, Ph.D., Brno, Veveří, CZ
Mgr. Martin Šarbort, PhD., Brno, Žabovřesky, CZ
Mgr. Miroslava Holá, PhD., Brno, Židenice, CZ
Mgr. Jindřich Oulehla, Brno, Černá Pole, CZ
prof. Ing. Josef Lazar, Dr., Brno, Královo Pole, CZ
Ing. Pavel Konečný, Brno, Štýřice, CZ
Ing. Jan Kůr, Kyjov, CZ
Ing. Ondřej Číp, Ph.D., Brno, Nový Lískovec, CZ

(74) Zástupce:
Kania, Sedlák, Smola, s.r.o., Mendlovo náměstí 907/1a, 603 00 Brno, Staré Brno

(54) Název užitného vzoru:
Integrovaný laserový snímač délky pro kontaktní měření

CZ 33046 U1

Integrovaný laserový snímač délky pro kontaktní měření

Oblast techniky

Technické řešení se týká integrovaného laserového snímače délky pro kontaktní měření na bázi interferometru.

Dosavadní stav techniky

Při současném stavu techniky jsou pro kontaktní délkové snímání využívány zpravidla následující kategorie technik:

A) Indukčnostní snímače
B) Optická pravítka
C) Laserové interferometry

Principem indukčnostních snímačů je převod hodnoty magnetické indukce na vzdálenost. Výhodou je kompaktní a cenově efektivní provedení a dále okamžité absolutní odvození pozice. Nevýhodou je nižší přesnost, citlivost na elektromagnetické rušení a teplotu prostředí, velká relativní chyba a nutnost kalibrace.

Optická pravítka odvozují měřenou vzdálenost od integrovaného mechanického pravítka, jehož stupnice je opticky snímána. Výhodou je robustnost vůči vlivům prostředí a lepší přesnost než např. u indukčnostních snímačů. Nevýhodou je nákladnější a objemnější konstrukce, relativní rozlišení polohy, které vyžaduje přítomnost referenčních značek a pro přesná měření nutnost kalibrace.

Laserové interferometry představují nejpřesnější techniky měření, jejichž výhodou je vysoké rozlišení, malá relativní chyba v závislosti na měřené délce a možnost přímé metrologické návaznosti na definici jednotky jeden metr dle prováděcích doporučení SI. Nevýhodou je potřeba složitého optického uspořádání, které je velmi citlivé na mechanické a teplotní vlivy okolí.

Podstata technického řešení

Výše uvedené nevýhody dosavadního stavu techniky jsou do značné míry eliminovány integrovaným laserovým snímačem délky, který obsahuje

- tělo opatřené vstupem pro připojení optického vlákna,

- dělič svazku paprsků, který je uspořádaný v těle a který obsahuje dělicí plochu pro dělení svazku paprsků přiváděného ze vstupu na měřicí část svazku a referenční část svazku,

- nosič, který je svým proximálním koncem suvně uložený v těle,

- zpětný odražeč, a je upevněný v nosiči, a

- odraznou plochu, která je uspořádána v těle,

přičemž vstup pro připojení optického vlákna, dělič, zpětný odražeč, odrazná plocha jsou uspořádány

- pro vedení měřicí části svazku paprsků do zpětného odražeče a její odražení zpět na dělicí plochu a pro vedení alespoň první části této odražené měřicí části do vstupu pro připojení optického vlákna,

- pro vedení referenční část svazku paprsků na odraznou plochu a její odražení zpět na dělicí plochu a pro odražení alespoň první části této odražené referenční části do vstupu pro připojení optického vlákna, a

- pro vytváření prvního rekombinovaného svazku paprsků z první části měřicí části svazku a první části referenční části svazku.

V přednostním provedení integrovaný laserový snímač dále obsahuje kolimační čočku, která je uspořádaná v těle mezi vstupem pro připojení optického vlákna a děličem svazku paprsků, přičemž je uspořádána pro kolimaci svazku paprsků přiváděných ze vstupu do děliče svazku paprsků a pro kolimaci prvního rekombinovaného svazku paprsků před jeho vstupem do vstupu pro připojení optického vlákna.

S výhodou je děličem dělicí hranol a/nebo je odrazná plocha tvořena odraznou optickou vrstvou deponovanou na boční ploše děliče.

Rovněž je výhodné, když je nosič na distálním konci opatřený kontaktním hrotem.

Přednostně je zpětný odražeč kulový zpětný odražeč a/nebo je vyroben z materiálu, jehož index lomu je roven 2 (± 0,05).

Ve zvlášť výhodném provedení je zpětným odražečem kulová čočka, která je na straně přivrácené k děliči opatřená antireflexní vrstvou a/nebo je na straně odvrácené od děliče opatřená odrazným povlakem.

Kolimační čočkou je nejlépe gradientní čočka.

Tělo je s výhodou vyrobeno z vrstveného kevlaru.

Integrovaný laserový snímač s výhodou obsahuje optického vlákno připojené ke vstupu pro přivádění svazku paprsků do děliče a pro odvádění rekombinovaného svazku.

Integrovaný laserový snímač podle tohoto technického řešení s výhodou obsahuje pomocný výstup, přičemž kolimační čočka, dělič, zpětný odražeč a odrazná plocha jsou vzhledem k pomocnému výstupu uspořádány

- pro odražení druhé části měřicí části svazku paprsků, která byla odražena od zpětného odražeče na dělicí plochu, do pomocného výstupu, a

- pro průchod druhé části referenční části svazku paprsků, která byla odražena od odrazné plochy na dělicí plochu, do pomocného výstupu, a

- pro vytváření druhého rekombinovaného svazku paprsků z druhé části měřicí části svazku a druhé části referenční části svazku.

Předkládané řešení kombinuje dílčí výhody jednotlivých metod: jednoduché, kompaktní, robustní a cenově efektivní optické uspořádání, které poskytuje velmi přesné rozlišení a metrologickou návaznost.

Objasnění výkresů

Technické řešení je dále podrobněji popsáno pomocí příkladného provedení, které je schematicky znázorněno na výkrese.

Příklad uskutečnění technického řešení

Příkladné provedení integrovaného laserového snímače délky pro kontaktní měření podle tohoto technického řešení obsahuje tělo 1 integrovaného laserového snímače, na jehož jednom konci je vstup pro připojení optického vlákna 8 a na druhém konci je kontaktní hrot 3.

Tělo 1 integrovaného laserového snímače délky je přednostně vyrobeno z vrstveného kevlaru, nejlépe z kevlaru vrstveného tak, že má koeficient tepelné roztažnosti menší než $10^{-6}\,K^{-1}$. Případně může být z jiného materiálu s nízkou hodnotou koeficientu teplotní roztažnosti.

Kontaktní hrot 3 je uspořádán na nosiči 4, který je suvně pomocí lineárního vedení 2 uložen v těle 1 integrovaného laserového snímače délky tak, že ho lze částečně vysouvat z těla 1 integrovaného laserového snímače a alespoň částečně zasouvat do těla 1 integrovaného laserového snímače délky.

Lineární vedení 2 je přednostně ve formě kuličkového lineárního vedení. Přednostně jsou rovněž tělo 1 a/nebo nosič 4 opatřeny neznázorněnými dorazy pro vymezení maximálního a/nebo minimálního vysunutí/zasunutí nosiče 4 z/do těla 1 integrovaného laserového snímače. Dále může být integrovaný laserový snímač opatřen neznázorněným předpínacím prvkem pro předepnutí nosiče 4 do maximální vysunuté polohy nebo maximální zasunuté polohy.

V nosiči 4 je upevněn zpětný odražeč 5 ve formě kulové čočky. Ve znázorněném příkladném provedení je zpětný odražeč 5 vyroben z dopovaného skla, které má index lomu prostředí blízký hodnotě 2, například ze skla dopovaného lanthanoidy. Na straně přivrácené ke kontaktnímu hrotu 3 je odražeč 5 ve formě kulové čočky povrstvený odraznou optickou vrstvou, což zvyšuje efektivitu odrazu, na druhé straně, tedy na straně přivrácené k přiváděnému svazků paprsků, je povrstvený antireflexní vrstvou, což eliminuje optické etalonové efekty uvnitř čočky.

V těle 1 integrovaného laserového snímače je dále mezi zpětným odražečem 5 a vstupem pro přivádění svazku paprsků, respektive pro připojení optického vlákna 8, uspořádán dělič 6 svazku paprsků a kolimační čočka 7.

Jako dělič 6 svazku je přednostně použit nepolarizující dělící hranol, u kterého není dělící poměr ovlivněn změnou polarizace (ke které může docházet primárně tím, že přívod svazku je realizován optickým vláknem).

Jako odrazná plocha je s výhodou použita odrazná optická vrstva 10, která je přednostně nanesená přímo na stěně děliče 6 svazku paprsků ve formě dělícího hranolu, což eliminuje nutnost prostorového sesouhlasení děliče 6 svazku paprsků a odrazné optické vrstvy 10 a snižuje prostorové nároky.

Jako kolimační čočka 7 je s výhodou použita gradientní čočka (čočka s proměnným indexem lomu, resp. čočka typu GRIN).

Dělič 6 svazku a/nebo kolimační čočka 7 mohou být uspořádány v těle 1 integrovaného laserového snímače fixně, nebo mohou být přestavitelné, čímž je umožněno pozdější doladění prostorového uspořádání.

Znázorněný integrovaný laserový snímač pracuje následovně:

Laserový svazek paprsků je přiváděn optickým vláknem 8 do integrovaného laserového snímače, konkrétně do kolimační čočky 7. Svazek vystupující z kolimační čočky 7 je přiváděn na dělič 6 svazku, ve kterém je svazek rozdělen tak, že se referenční část RB svazku odrazí od dělicí plochy 9 na odraznou optickou vrstvu 10, ze které se odrazí zpět na dělicí plochu 9 a z ní je první část referenční části RB svazku odražena zpět do kolimační čočky 7, zatímco druhá část referenční části RB svazku projde dělicí plochou 9 do pomocného výstupu 11. Měřicí část MB svazku projde dělicí plochou 9 děliče 6 svazku a dopadá na zpětný odražeč 5, ze kterého se odrazí zpět do děliče 6 svazku, resp. na dělicí rovinu děliče 6 svazku, ze kterého dále pokračuje první část měřicí části MB svazku do kolimační čočky 7 a druhá část do pomocného výstupu 11.

První část odražené měřicí části MB a první část odražené referenční části RB svazku, které dopadají na dělící plochu 9, se v místě dopadu rekombinují (znovu spojují) a dochází zde k interferenci těchto částí MB, RB, tj. vzniká první rekombinovaný/interferenční svazek, který je přiváděn do kolimační čočky 7. První rekombinovaný svazek představuje interferenční signál, který nese informaci o vzájemné fázi referenční části RB svazku a měřicího části MB svazku, ze které lze odvodit relativní polohu lineárního vedení 2 a potažmo kontaktního hrotu 3 vzhledem k děliči 6 svazku.

Druhá část odražené měřicí části MB svazku a druhá část odražené referenční části RB svazku, které dopadají na dělící plochu 9, se v místě dopadu rovněž rekombinují (znovu spojují) a dochází zde k interferenci těchto částí MB, RB, tj. vzniká druhý rekombinovaný/interferenční svazek, který je přiváděn do pomocného výstupu 11.

Druhý rekombinovaný svazek je využitelný zejména při mechanické kompletaci, resp. seřizování optické sestavy integrovaného laserového snímače.

Díky výše popsanému uspořádání představuje jediné rozhraní mezi integrovaný laserovým snímačem, zdrojem laserového svazku a systém pro vyhodnocení interferenční fáze jedno optické vlákno, což eliminuje vliv elektromagnetického rušení, neboť přenos informace se děje plně fotonicky (bez přítomnosti elektroniky).

Díky použití kolimační čočky 7 ve formě gradientní čočky je umožněno generování vhodného profilu svazku přiváděného do děliče 6 a zároveň je umožněno s vysokou účinností zpětně navázat interferenční signály zpět do optického vlákna 8.

Díky tomu, že je jako zpětný odražeč 5 použita kulová čočka z dopovaného skla, odráží zpětný odražeč 5 svazek tak, že osy dopadajícího a odraženého svazku jsou rovnoběžně, čímž se v kombinaci s kolimační čočkou 7 ve formě gradientní čočky kompenzuje případná úhlová chyba lineárního vedení. Díky kulovitému tvaru zpětného odražeče 5 je na rozdíl od běžných odražečů možné odrážet svazek paprsků tak, že osy dopadajícího a odraženého svazku jsou identické, což umožňuje využít jedno optické vlákno 8 a jednu kolimační čočku 7 jak pro přívod svazku laserových paprsků, tak pro výstup zpětně odraženého, rekombinovaného interferenčního signálu.

Samotný princip měření, při kterém se měřená délka odvozuje od optické frekvence laserového svazku, umožňuje přímou metrologickou návaznost na jeden metr dle definice SI.

Ačkoli byla popsána zvlášť výhodná příkladná provedení, je zřejmé, že odborník z dané oblasti snadno nalezne další možné alternativy k těmto provedením. Proto rozsah ochrany není omezen na tato příkladná provedení, ale spíše je dán definicí přiložených nároků na ochranu.

NÁROKY NA OCHRANU

1. Integrovaný laserový snímač délky pro kontaktní měření, **vyznačující se tím**, že obsahuje

- tělo (1) opatřené vstupem pro připojení optického vlákna (8),

- dělič (6) svazku paprsků, který je uspořádaný v těle (1) a který obsahuje dělicí plochu (9) pro dělení svazku paprsků přiváděného ze vstupu na měřicí část (MB) svazku a referenční část (RB) svazku,

- nosič (4), který je svým proximálním koncem suvně uložený v těle (1),

- zpětný odražeč (5), který je upevněný v nosiči (4), a

- odraznou plochu, která je uspořádána v těle (1),

přičemž vstup pro připojení optického vlákna (8), dělič (6), zpětný odražeč (5), a odrazná plocha jsou uspořádány

- pro vedení měřicí části (MB) svazku paprsků do zpětného odražeče (5) a její odražení zpět na dělicí plochu (9) a pro vedení alespoň první části této odražené měřicí části (MB) do vstupu pro připojení optického vlákna (8),

- pro vedení referenční část (RB) svazku paprsků na odraznou plochu a její odražení zpět na dělicí plochu (9) a pro odražení alespoň první části této odražené referenční části (RB) do vstupu pro připojení optického vlákna (8), a

pro vytváření prvního rekombinovaného svazku paprsků z první části měřicí části (MB) svazku a první části referenční části (RB) svazku.

2. Integrovaný laserový snímač podle nároku 1, **vyznačující se tím**, že dále obsahuje kolimační čočku (7), která je uspořádaná v těle (1) mezi vstupem pro připojení optického vlákna (8) a děličem (6) svazku paprsků, přičemž je uspořádána pro kolimaci svazku paprsků přiváděných ze vstupu do děliče (6) svazku paprsků a pro kolimaci prvního rekombinovaného svazku paprsků před jeho vstupem do vstupu pro připojení optického vlákna (8).

3. Integrovaný laserový snímač podle kteréhokoli z předcházejících nároků, **vyznačující se tím**, že dělič (6) je dělicí hranol a/nebo odrazná plocha je tvořena odraznou optickou vrstvou (10) deponovanou na boční ploše děliče (6).

4. Integrovaný laserový snímač podle kteréhokoli z předcházejících nároků, **vyznačující se tím**, že nosič (4) je na distálním konci opatřený kontaktním hrotem (3).

5. Integrovaný laserový snímač podle kteréhokoli z předcházejících nároků, **vyznačující se tím**, že zpětný odražeč (5) je kulový zpětný odražeč a/nebo je vyroben z materiálu, jehož index lomu je roven 2 (± 0,05).

6. Integrovaný laserový snímač podle kteréhokoli z předcházejících nároků, **vyznačující se tím**, že zpětný odražeč (5) je kulová čočka, která je na straně přivrácené k děliči (6)

opatřená antireflexní vrstvou a/nebo je na straně odvrácené od děliče (6) opatřená odrazným povlakem.

7. Integrovaný laserový snímač podle kteréhokoli z předcházejících nároků, **vyznačující se tím**, že kolimační čočka (7) je gradientní čočka.

8. Integrovaný laserový snímač podle kteréhokoli z předcházejících nároků, **vyznačující se tím**, že tělo (1) je vyrobeno z vrstveného kevlaru.

9. Integrovaný laserový snímač podle kteréhokoli z předcházejících nároků, **vyznačující se tím**, že obsahuje optického vlákno (8) připojené ke vstupu pro přivádění svazku paprsků do děliče (6) a odvádění rekombinovaného svazku.

10. Integrovaný laserový snímač podle kteréhokoli z předcházejících nároků, **vyznačující se tím**, že obsahuje pomocný výstup (11), přičemž kolimační čočka (7), dělič (6), zpětný odražeč (5) a odrazná plocha jsou vzhledem k pomocnému výstupu (11) uspořádány

- pro odražení druhé části měřicí části (MB) svazku paprsků, která byla odražena od zpětného odražeče (6) na dělicí plochu (9), do pomocného výstupu (11), a

- pro průchod druhé části referenční části (RB) svazku paprsků, která byla odražena od odrazné plochy na dělicí plochu (9), do pomocného výstupu (11), a

- pro vytváření druhého rekombinovaného svazku paprsků z druhé části měřicí části (MB) svazku a druhé části referenční části (RB) svazku.

1 výkres

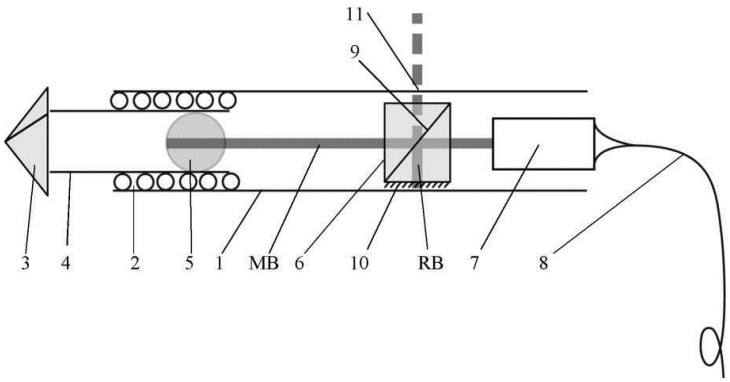

Obr. 1

Appendix 5

Optics and Lasers in Engineering 141 (2021) 106568

Contents lists available at ScienceDirect

Optics and Lasers in Engineering

journal homepage: www.elsevier.com/locate/optlaseng

Compact differential plane interferometer with in-axis mirror tilt detection

Šimon Řeřucha*, Miroslava Holá, Martin Šarbort, Jan Hrabina, Jindřich Oulehla, Ondřej Číp, Josef Lazar

Institute of Scientific Instruments of the Czech Academy of Sciences (ISI), Kralovopolska 147, 612 64 Brno, Czech Republic

ARTICLE INFO

PACS:
07.60.Ly
06.30.Bp
42.62.Eh
07.60.-j
42.15.Eq

Keywords:
Laser interferometry
Optical metrology
Dimensional measurement
Common path interferometer
Differential interferometer
Tilt compensation

ABSTRACT

Besides the environmental fluctuations, the typical sources of significant uncertainty in the laser interferometry systems are the geometrical errors. These are stemming, among others, from the misalignment of measurement axes, the thermo-mechanical influences of the system components and the mounting, guidance errors of the translation mechanism that carries the measurement mirror or vibrations. We report on a compact double-pass differential plane interferometer that features an original optical arrangement with four parallel and coplanar beams, where the beam pairs in the two arms are coaxial. The differential arrangement minimizes the dead path and shortens the metrological loop so that the sensitivity to thermal drifts and vibrations is reduced. The arm symmetry allows for the preservation of the Abbe principle, and the common path mitigates the influences of the environmental disturbances. The interferometer optics is designed as a self-contained single-piece assembly made using optical contacting from the low-expansion materials. The interferometer system integrates the homodyne receiver (even though the optical arrangement is well-suited for heterodyne detection too) and also a tilt-detection electronics that allows for detection of pitch and roll of the interferometer mirror so that the parasitic movement of the measuring mirror could be compensated for. The experimental characterization revealed a good optical performance of the interferometer with sub-nanometre cyclic error and the resolution of tilt detection in order of a few microradians.

1. Introduction

Establishing a well-performing measurement testbed with a laser interferometer, the wide-spread workhorse in the geometric and dimensional metrology [1–3], means to address a quite well-known list of issues [4]. In the first place, all three integral parts of any interferometric system – the laser source, the optics, and the phase-detection system (receiver) – have to be up to quite a high degree of precision and well-characterized (calibrated), especially when it comes down to preserving the traceability link [5]. The laser source has to deliver sufficient stability of the optical frequency, and the optics in conjunction have to exhibit a minimal cyclic error [6–9]. Then there are the environmental factors that need to be tackled, i.e., a priori minimized when applicable or observed and compensated for otherwise.

Apart from the fluctuations in the refractive index of air, that are typically compensated for using the monitoring of atmospheric conditions [10–13], by tracking refractometry [14] or by avoiding the air either partially or entirely [15,16], it is the mechanical stability of the whole arrangement that is the most significant source of uncertainty. In the first line, a stable metrology reference frame is critical for high-precision instrumentation in the dimensional metrology and nanometrology [17–19] to keep the metrology loop under control, and the amount of used expensive Zerodur ceramics or Invar alloy determines the quality and precision of the final instrument. Next issue, typically associated (and almost unavoidable) with the displacement interferometers, is the mechanical imperfection of the translation mechanism that carries the measurement mirror. The resulting guidance errors give rise to the cosine and Abbe errors [4].

A feasible approach is using a differential arrangement with parallel beams in the two interferometer's arms. To a certain extent, the differential approach excludes the body of the interferometer from the metrological loop. The observed phase shift is dependent only on the mutual position of the two arms' mirrors along the common measurement axis. Relatively few interferometers of such an arrangement has been described for geometric measurements [20–22], coordinate measurements [23] or specialized application such as scanning probe microscopy [24,25]. Several differential interferometers are also available commercially, such as the RLD10-xx-DI series by Renishaw, DPMI by Zygo, or the 10719A and 10715A by Keysight.

Generally, the parallel beams have a positive impact on the reduction of the optical path-length change due to uniform changes in the refractive index of air or thermal expansion of the instrumentation base (in a

* Corresponding author.
E-mail address: res@isibrno.cz (Š. Řeřucha).

https://doi.org/10.1016/j.optlaseng.2021.106568
Received 15 April 2020; Received in revised form 15 November 2020; Accepted 2 February 2021
Available online 15 February 2021

similar manner to the compensated arrangement for the interferometer back-to-back comparisons [26]). When considering the sensitivity to the geometrical errors, such as the guidance errors or parasitic pitch/yaw of the measured axis, it is the beam arrangement that plays an important role.

Reliable preservation of the Abbe principle requires the interferometer's axes to be not only parallel but also coaxial, which in turn enforces a double-pass configuration. Suitable interferometers are for example the PTB interferometer [20], NPL Differential Plane Interferometer [27,28], its principally close commercial relative DPMI (Zygo) or 10715A (Keysight). These interferometers have the four beams either coplanar and evenly spaced, where the inner pair and the outer pair represent the two arms or organized in a 2x2 matrix with the beams from respective arms on the diagonals. What remains is the cosine error, that typically occurs due to the imperfect motion of the measurement mirror resulting in its residual tilt (pitch and yaw) that occur both statically (e.g., from guiding errors) and dynamically (e.g., from vibrations).

In this paper, we present a four beam double-pass differential plane interferometer with coplanar beams and coaxial arms, that combines an original optical arrangement and the ability to detect the tilt of the measurement mirror. The interferometer optics is arranged and realized as a self-contained, compact single block without the need for an external beam-splitting element and assembled using the optical contacting to increase the thermo-mechanical and alignment stability of the optical elements.

The arrangement also allows us to introduce the detection of lateral displacement of the beam in one of the interferometer arms with a position-sensitive detector so that any changes in the tilt of the respective mirror could be detected *in-situ*, simultaneously with the phase measurement and with real-time response. As the response of the lateral shift scales with the physical distance, it might be slightly impractical for the inference of the absolute tilt angle, but well exploitable for the realization of a closed-loop compensation of the tilt, for instance using the wide-spread piezoelectric adjusters.

The in-line tilt detection feature could be considered a significant advantage in comparison with alternative approaches. Most usually an additional interferometer axis (or axes for up to six degrees of freedom characterization) is used [17,18,29–32] (which is costly). A different approach might be, for example, a CCD-assisted alignment [33] (which probably will not keep pace with the phase measurement) or in-situ estimation through physically "modulating" the pitch and yaw [34] (that require repeated measurement).

In the following sections, we describe the architecture and optical arrangement (Section 2) and the tilt sensing approach (Section 3), present the characterization (Section 4) and discuss the aspects of the presented system (Section 5) before concluding the article (Section 6).

2. The interferometer

The architecture of the interferometer is shown in Fig. 1. The heart of the optical arrangement is the large polarizing beam splitter (PBS) that distributes the input laser beam into four parallel beams in a single plane. With the first incidence of the input laser beam on the beam-splitting layer, this is split into two beams, forming the two polarization-separated arms of the interferometer. The reflected part exits the interferometer as the first-pass beam of the outer pair. The transmitted part undergoes a reflection on the auxiliary corner cube (CC), bounces back from the dielectric reflective coating on the opposite side, passing twice the quarter-wave plate (QWP), and then reflects on the splitting layer and exits the interferometer as the first-pass beam of the inner pair.

Both beams pass the other QWP once after exiting the PBS, and once after bouncing back from plane surfaces, then re-enter the interferometer, undergo a reflection on the rear CC, and exit the interferometer as the second-pass beams. After the second round-trip, the returning inner beam carries on with the voyage bouncing from the QWP on the right side, where a small part of the beam is transmitted and illuminates the position-sensitive detector that allows for the sensing of the tilt of the surface that reflects the inner beam. It then passes the other small CC and joins the outer beam on its return from the second pass at the beam-splitting plane. From here, the recombined (and still polarization-separated) beams continue hand-in-hand towards the four-diode homodyne receiver.

To achieve maximal thermo-mechanical stability of the optical arrangement, depicted in Fig. 2, the components were manufactured from fused silica (bulk components) and crystal quartz (retardation plates), that have low and approximately matching coefficient of thermal expansion. The components, coated with anti-reflection coatings, were assembled using the optical contacting technology. The optical assembly ($56 \times 51 \times 12$ mm) was enclosed in a titanium housing ($94 \times 60 \times 30$ mm), which also contained the phase receiver, the position-sensitive detection facility and a collimator slot for a convenient optical fibre light delivery.

The homodyne receiver, principally described, e.g., in [35], used a four-detector arrangement and incorporated an active preamplifier. For the tilt sensing, the four-quadrant photodiode (Hamamatsu S4349) was installed, also with a preamplifier. Both transistor-based amplifiers were designed as low-power and low-dissipation circuits.

3. Tilt sensing

The tilt detection feature in the interferometer system exploits the internal reflection at zero degrees that occurs in the path of the inner arm, apparent from Fig. 1. When the respective mirror is tilted by the angle of φ, as illustrated in Fig. 3, the beam in the inner path is deflected by 2φ on its first incidence with the mirror. Back on the rear plane of the large beam-splitter, the pivot plane, the projection of the beam is laterally shifted by $d_x = L_a \tan(2\varphi)$, where L_a is the distance between the pivot plane and the mirror. When the beam passes the corner cube, its tilt is unchanged, and it is laterally shifted by $-d_x$. After the second reflection on the mirror, the beam path is again parallel to that of the original beam and laterally displaced by $2d_x$. Consequently, the tilt sensing is insensitive to the spacing between the optics and the position detector, but the absolute value of the beam displacement is proportional to the distance between the optics and the mirror.

The position-sensitive detector in our system features four square-shaped photo-sensitive segments in a 2×2 matrix. When the beam illuminates the four-quadrant detector, a shift of the incident beam's axis from the detector's area affects the incident power on the individual segments q_1, q_2, q_3, q_4. Using the traditional interrogation approach, we calculate

$$S = q_1 + q_2 + q_3 + q_4 \tag{1}$$

$$D_x = [(q_1 + q_4) - (q_2 + q_3)]/S \tag{2}$$

$$D_y = [(q_1 + q_2) - (q_3 + q_4)]/S \tag{3}$$

to obtain tilt signals D_x, D_y that correspond to the tilt in $x-$ and $y-$axes. These sigmoid-shape signals, normalized by the total incident intensity S, have a range of $[-1, 1]$, and their slope and definition range is a function of the beam radius, the beam profile, the L_a distance affected by tilt and L the total distance the beam travels from the waist to the detector (when the mirrors are perfectly aligned).

We can roughly estimate the waveform with a simple numerical model. Assume the mirror is tilted by α, β in the $x-$ and $y-$axes. Then on the detector, the incident beam has the offset x_0, y_0 from the center

$$x_0 = 2L_a \tan(2\alpha) \tag{4}$$

$$y_0 = 2L_a \tan(2\beta) \tag{5}$$

and the beam path length z will be

$$z = L - 2L_a + \sqrt{4L_a^2 + x_0^2 + y_0^2} \tag{6}$$

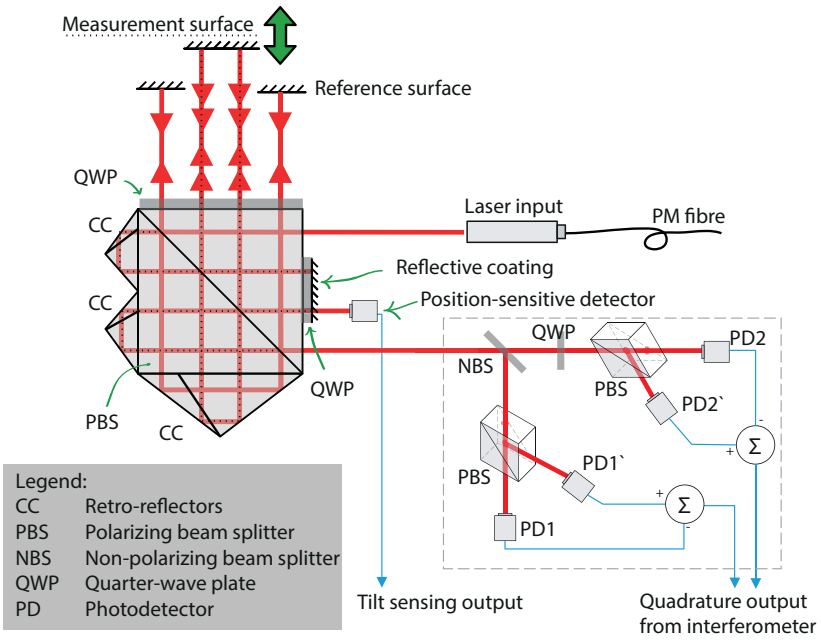

Fig. 1. The architecture of the interferometer system: the optical arrangement creates four parallel beams in a single plane, reflected from a pair of plane surfaces, where the inner pair and the outer one represent the two arms (the beam path in the inner arm is emphasised with the fine dots).

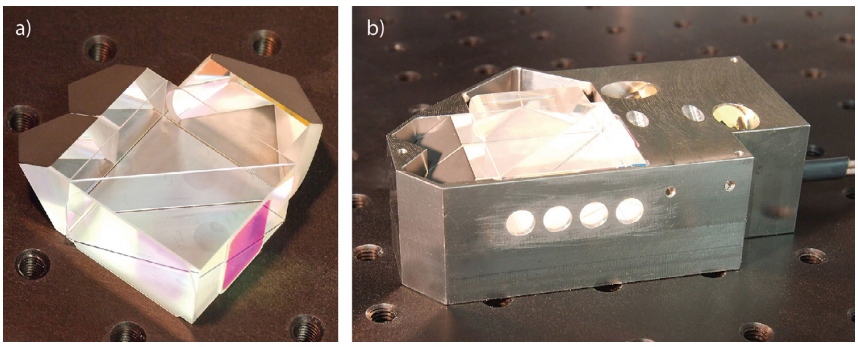

Fig. 2. The interferometer optics assembled (a) and mounted in the housing (b) – provisional housing from aluminium is depicted.

Knowing the wavelength λ of the Gaussian beam with the waist radius of w_0, we can express the actual radius depending on the distance z

$$w(z) = w_0\sqrt{1+\left(\frac{z}{z_r}\right)^2} \tag{7}$$

where $z_r = \pi w_0^2/\lambda$ is the Rayleigh length. The beam intensity at particular point (x, y) can be expressed as

$$I(x,y) = I_0\left(\frac{w_0}{w(z)}\right)^2 \exp\left[\frac{-2((x-x_0)^2+(y-y_0)^2)}{w(z)^2}\right] \tag{8}$$

where I_0 is peak intensity.

By integrating the function over the range given by the physical dimensions of the photodetector segments, we obtain the desired waveform. An example, based on real parameters of our experimenal setting, is depicted in the later section in Fig. 6a.

4. Characterization

To characterize the performance of our design, we present both an empirical assessment (Sections 4.3 and 4.4) and an experimental investigation. We have carried out two (sets of) experiments: one focused on assessing the periodic nonlinearity (Section 4.1) and the other on the tilt sensing (Section 4.2). In the first scenario, we introduced a periodical displacement of the reference mirror with a linear translation stage and used frequency decomposition to investigate the amplitude of the periodic nonlinearities. In the second experiment, we observed the angle between the interferometer mirror simultaneously with the tested interferometer and an autocollimator and compared the results with the theoretical prediction from the previous section.

4.1. Investigating the scale linearity

For the investigation of the cyclic errors (see Fig. 4a) we used the laser interferometer in conjunction with a pair of round silver mirrors. The first mirror, referred to as the measurement mirror, with a diameter of 12.7 mm reflected the inner pair of beams and was mounted on a PZT translation stage (Thorlabs MAX312D/M). The reference mirror, used for the outer pair, was a 50.8 mm diameter mirror with 13.5 mm circular cut-away.

The PZT stage was driven with a signal generator producing voltage steps corresponding to ≈ 5 nm displacement in 1.22 μm range (covering slightly over seven interference fringes). A frequency stabilized and iodine locked diode laser [36] with optical fiber-coupled output

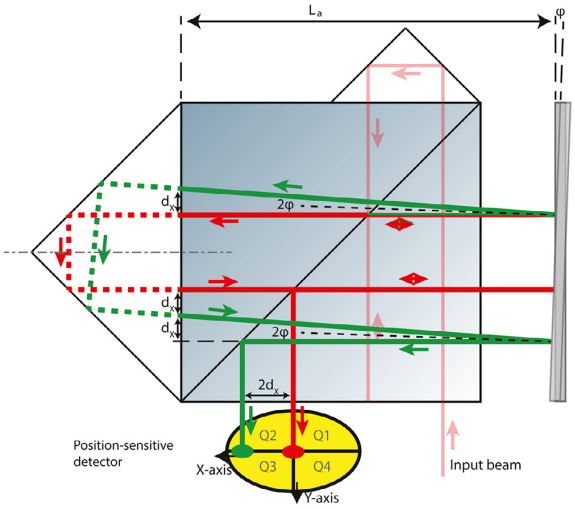

Fig. 3. The effect of mirror tilt to the beam path in the interferometer: the tilt of the mirror causes only a lateral displacement of the beam and not a tilt.

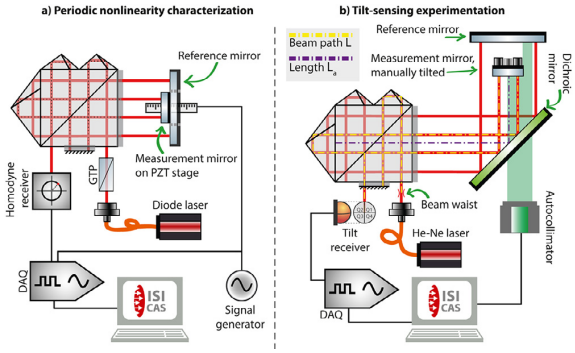

Fig. 4. The experimental setups for the characterization of periodic nonlinearities (a) and the proof-of-concept tilt-sensing experimentations (b); the beam path L denotes the total length the beam travels from the waist through the inner arm of the interferometer to the position-senstive detector and the length L_a is the distance affected by tilt of the measurement mirror.

served as a source for the interferometer. The prototype of the interferometer we used for the experimentation was adjusted for the input power of 0.25 mW, which resulted in ≈ 40 μW power on each photodiode in the receiver. Before entering the interferometer, the laser beam polarization was filtered with a Glan-Taylor calcite polarizer. The output from the interferometer was converted into voltage signals with the four-photodiode homodyne receiver. These signals were consequently recorded and preprocessed with our custom interferometer module (DETINF card by ISI) with 0.5 kHz output frequency and simultaneously sampled 12-bit analog inputs.

On the recorded signals, we applied the elliptical correction [6] and extracted the interference phase. Then we averaged the read displacement for individual steps and removed the trajectory of the PZT with a polynomial.

Fig. 5 shows that without the elliptical correction the interferometer exhibits a periodic nonlinearity < 0.55 nm. With the correction applied, the residuals generally keep below ± 0.1 nm ($\sigma = 0.055$ nm); we attribute the outliers to the environmental factors. Such a performance closely follows the state of art in the interferometry, with currently recognized non-linearity limit at 5 pm and resolution figure at 0.1 nm [2].

Clearly, the technique we used has its limitations, and further experimentation would be need to investigate the limits of the non-linearity and possibly enhance the post-processing scheme to push the performance closer to the current state-of-art. The next step forward would be a calibration against a suitable closed-loop controlled system, for instance, the X-ray interferometry [37].

4.2. Testing the tilt detection

For the experimental investigation of the tilt sensing, we used interferometer together with the pair of mirrors and a reference autocollimator, as sketched in Fig. 4b. As the source, we used a frequency stabilized single-mode He-Ne laser with fiber-coupled output with the nominal diameter of the feeding beam of 4 mm. The position-sensing detector with active surface of 3×3 mm received only the small fraction (0.3 μW) that passed through the coating (as this was designed for maximal reflectivity) on the small wave-plate. With the use of a dichroic mirror, we arranged the setup so that we were able to manually tilt the mirror and simultaneously observe the tilt with both the reference system and the interferometer under test. The active length of the beam path between was $L_a = 190$ mm and the total path was $L = 959$ mm. The four signals from the position-sensitive detector were recorded with our custom mixed-signal module (ADDA3g card by ISI) with 0.5 kHz sampling frequency, and 12-bit analog inputs.

Before the measurement procedure, the mirrors were aligned to obtain an interferogram with the best contrast. Their parallelity was checked with the autocollimator, whose gauges were reset to a zero angular position.

During the actual measurement, we manually adjusted the mirror pitch between zero and 850 μrad stepwise with 120 μrad increments, then adjusted back to zero, then we went in the other direction to 850 μrad and back to zero (please note the range and steps are approximate as the measuring instrument operated with arc seconds, i.e. we used ± 175 asec range with 25 asec steps). For each pitch, we took ≈ 1000 readings of the signals of interest.

The outcomes are summarized in Fig. 6. Fig. 6a shows the theoretically predicted course of the tilt signal m_y overlapped with the experimentally obtained curve c_y. The plot also shows a linear fit of the nearly-linear middle section of the predicted signal (in the range of ± 1000 μrad) – the slope of this linear fit indicates that for particular configuration in the sensitivity of the tilt measurement is approximately $0.48 \cdot 10^{-3}$ μrad^{-1}.

The difference $c_y - m_y$ between the experimental data and theoretical prediction, shown in Fig. 6b, falls below 0.02 in the ± 1000 μrad region, which indicates approximate accuracy (in terms of linearity error) below 41.3 μrad. The standard deviation of readings at particular points, shown in Fig. 6c, indicates the precision of reading $\sigma < 5.7$ μrad).

It is apparent that the accuracy of the tilt detection does not reach the figures achievable with the additional interferometer axis (or interferometer with the multiaxis arrangement; typically around 1 μrad [31,32]). With the current state, the most limiting factor is probably the amount of light incident to the position-sensitive detector and associated noise from amplification of the weak signals. We expect the figure would improve when the position-sensitive detector operates with higher incident power than we have available now, which involves redesigning the reflective optical coatings.

The significant advantage of our approach is that the tilt is detected without this added axis (which is convenient in terms of cost and space). It also does not pose additional requirements (and uncertainty sources) such as the geometrical properties of the reflectors, their mutual organization or uneven influence of the atmospheric perturbances.

4.3. Measurement capability

With the experimental results at hand, we are able to characterize the measurement capability of the proposed interferometer system:

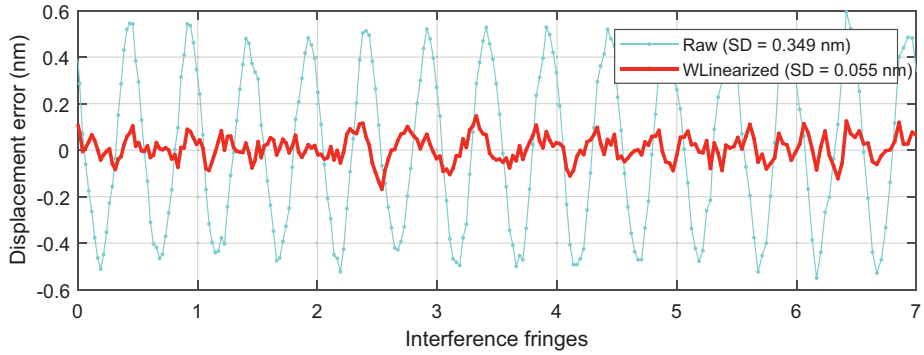

Fig. 5. The periodical non-linearity residuals of the interferometer.

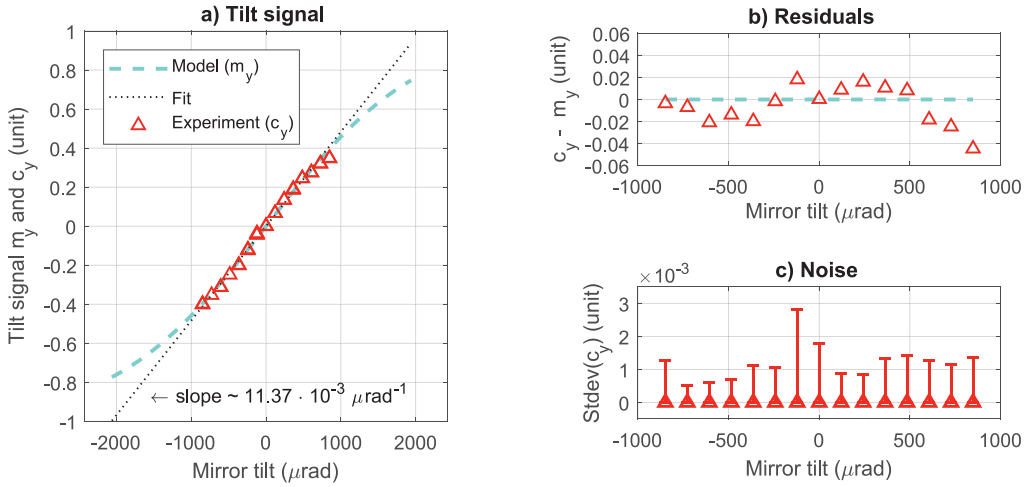

Fig. 6. The tilt-detection output curve: dashed line shows theoretically modelled shape and triangles show experimental observations (a); the coincidence of the model and the experimental outcomes (b); the fluctuations of the tilt reading (c).

Displacement resolution is principally limited by the fringe subdivision approach. For the homodyne detection the resolution is typically given by the performance of the consequent analogue-digital conversion of the signals from the homodyne receiver; depending on the condition the limit lies at picometre level ([36], Section 2.3).

Displacement precision and accuracy are limited by several factors. A constant term involves: (a) the periodic non-linearity stemming mainly from manufacturing imperfections and parasitic polarization crosstalks, experimentally found to be 0.055 nm with our interferometer and (b) the noise floor (that also involves the processing electronics beyond the interferometer), that was found to be below 0.07 nm with 10 ms averaging (see Fig. 7).

Other factors are relative to the difference in the optical path length in the interferometer's arms L: (a) the environmental disturbances, manifesting as changes in the refractive index of air, typically controllable down to $1 \cdot 10^{-8} \cdot L$ and (b) the optical frequency stability of the laser source ($2 \cdot 10^{-8} \cdot L$ with a He-Ne laser).

Displacement range is principally limited by the coherence length of the laser source (hundreds of meters with the He-Ne lasers) and the adjustment of geometry of the laser beam and the interferometer's optics. In our previous work, we have demonstrated the measurement on a 3.5 m long calibration bench with the slightly different two-pass arrangement, but with identical beam collimation and very similar optical components [38]. It translates to 1.75 m range for the four-pass system, but it could be safely expected the range could be upscaled by a factor of ten.

The interferometric system from Rerucha et al. [38] also used identical homodyne receivers and we demonstrated the *displacement bandwidth* of up to 19 mm.s^{-1} which translates to 9.5 mm.s^{-1} for the four-pass system.

As for the tilt sensing performance, we are able to estimate the *tilt sensing precision and accuracy* and *tilt sensing range* using the experimentally obtained values. We have evaluated the precision to be 5.7 μrad and the accuracy to be 41.3 μrad. We assume the useful measurement range is $\pm$2000 μrad, where the sigmoid-shaped tilt signal has a reasonably detectable slope. We substitute these three angular values as α into the Eq. (4), effectively converting them onto the lateral shift of the laser beam on the surface of the position-sensitive detector x_0. Then we reorganise the Eq. (4) to express the angle α as a function of parameter L_a

$$\alpha = \frac{1}{2}\tan^{-1}\left(\frac{x_0}{2L_a}\right) \tag{9}$$

and substitute the respective values of x_0, we obtain the approximation of the precision, accuracy and range as a function of the distance L_a, shown in Fig. 8. For the minimal $L_a = 40$ mm (when the mirror is as close as possible to the interferometer housing) the measurement range will be the broadest (9.5 mrad) and the precision and accuracy the worst (190 and 27 μrad). At $L_a = 1$ m, the range decreases to mere

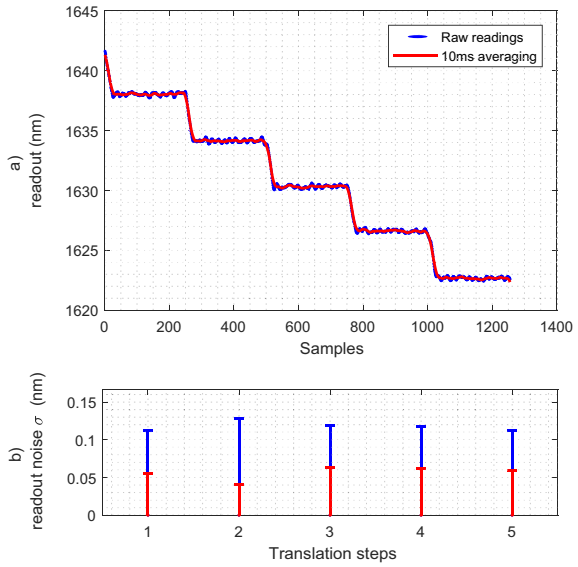

Fig. 7. Displacement readings from the interferometer during step-by-step translation demonstrate the 1σ noise below 0.15 nm with raw readings and below 0.07 nm with 10 ms averaging.

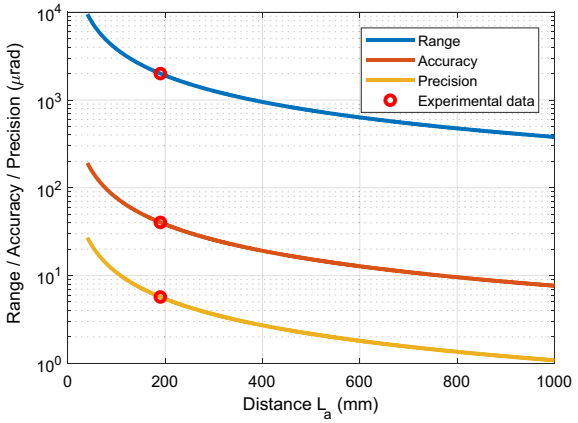

Fig. 8. The measurement range (a) and accuracy (b) of the tilt sensing as a function of distance L_a.

(380 μrad) and the precision and accuracy significantly improves (7.7 and 1.1 μrad). In other words, the signal-to-noise ratio (the accuracy to measurement range ratio) and the dynamic range (the precision to measurement range ratio) are constant. Similarly, the particular figures will also scale proportionally to the beam radius and its Rayleigh distance.

The *tilt sensing bandwidth* is directly related to the frequency response f_c of the position-sensitive detector and the preamplifier, that is in our case higher than 1 MHz.

A detailed characterization of the tilt sensing performance would require more experimentation, especially with the adjusted configuration of the reflective coating that would allow for more incident power on the position-sensitive detector. We estimate that this adjustment could improve the accuracy by a factor of 10, which would render the performance much close to that of interferometer-based angular measurements.

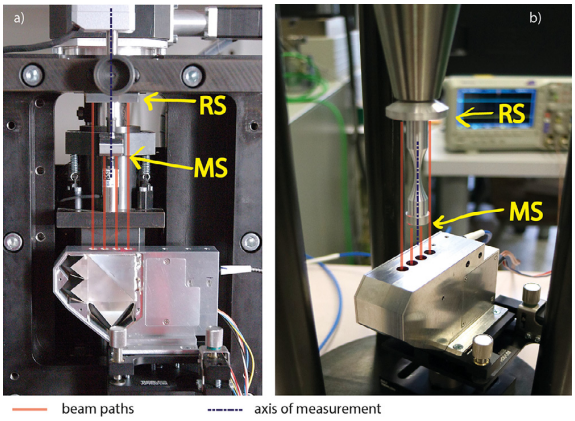

Fig. 9. Example application arrangements with the reference (RS) and measurement (MS) surface indicated: setup for calibration of 8−mm pencil-type length gauges (a) and setup for high-cycle material fatique characterization (b).

4.4. Application use cases, improvement over state-of-art

Due to a large amount of previously published interferometric systems for dimensional measurements [1–3], it is challenging to compare the presented systems in every aspect. Generally (as we mentioned in introductory section), the significant advantage of the presented interferometer is the compact and single-block form factor, that in combination with the four-beam coplanar differential arrangement and cube-corner retroreflectors in the beam paths delivers the principally most stable and geometry error-free operation for a wide range of measurement scenarios. Of course, there might be a slightly better performing approach for any of the scenario, but it will be probably significantly more complex and more application-specific.

Fig. 9 a) shows the interferometer mounted in a machine, designed for the calibration of 8-mm form-factor length gauges. This application could be perceived as a significantly simplified alternative, e.g. to the PTB nano-comparator [15] for industrial use. Any interferometer with other than the coplanar four-beam differential arrangement would bring increased measurement uncertainty because of geometric errors (Abbe errors, material thermal expansion). The existing interferometers with the right arrangement are bulkier. However, our interferometer brings additional advantage with the tilt sensing, that allows the system to compensate for the parasitic angular movement of the measuring mirror in the real-time.

Fig. 9 b) shows the interferometer mounted in an experimental arrangement used for measurement of high-cycle material fatigue. The material sample is subjected to a vibration load along the measurement axis (at ≈ 20 kHz) until the sample breaks apart. The interferometer evaluates the elongation of the sample, especially just before breaking. The frequency amplitude of the induced vibrations caused rapid phase-changes (interference fringes were observed with up to 25 MHz bandwidth) that were processed with dedicated electronics with 100 MHz. The requirement for such a high bandwidth would generally prevent the use of a heterodyne interferometer (again, except for some significantly more complex dedicated setup [39]). Here, a non-differential arrangement would cause problems with mechanical stability due to induced vibrations. The differential interferometers with the beams organized into the 2×2 matrix would be very difficult to align with the sample.

5. Discussion

The presented configuration passively compensates a small tilt of the measuring mirror with respect to the reference mirror in terms of

preserving the contrast of the interferograms. As both the measuring beam and the reference beam pass through a single large corner-cube reflector, the tilt of the mirrors only reduces the overlap of the beams from the two arms at the output. This results in a lower interference contrast but not in a tilt of the wavefronts.

The sensitivity and range of the tilt detection could be scaled by choosing a suitable distance between the interferometer's body and the mirrors (as mentioned before). Thanks to the differential and common-path arrangement, the physical placement does not add up to the dead-path thus does not increase the sensitivity to the environmental influences.

What could be seen as the Achilles heel is that the lengths of the beam paths "in glass" differ by ≈ 150 mm between the measuring and reference arms. This unbalance increases sensitivity of the interferometer to thermal expansion of the glass ($75\ \mathrm{nm{\cdot}K^{-1}}$) and thermal drift of the refractive index ($1.3\ \mu\mathrm{m{\cdot}K^{-1}}$) [40]. These effects are, on the other hand, significantly less severe thanks to the manufacturing out of fused silica with small temperature sensitivity ($0.52 \cdot 10^{-6}\ \mathrm{K^{-1}}$) and very low thermal conductivity ($1.38 \cdot 10^{-3}\ \mathrm{W{\cdot}K^{-1}}$). The unbalance of the beam paths also makes the interferometer susceptible to the frequency noise of the laser source, where 1 part per billion drift of the optical frequency will induce ≈ 150 pm drift.

Based on these findings, we have proposed a slightly modified arrangement, where the input beam would enter the optics at the point where the inner arm beam bounces for the first time from the small wave-plate. This wave plate will be replaced with two smaller ones, where one will remain in place where the part of the light is let through to the position-sensitive detector, and the other will be placed where the input beam initially entered the interferometer. Consequently, the geometric properties would remain intact, but the path will have equal length.

6. Conclusion

We presented the universal and compact design of a common-path displacement measuring interferometer with original optical arrangement suited for differential measurement with Abbe principle preservation. The interferometer system integrates the self-contained optics with the phase receiver and a facility for detecting the tilt of the one of its mirror in a compact package. The experimentation revealed the interferometer system has a periodic nonlinearity < 0.1 nm, and can detect the tilt of one of the mirrors with resolution down a few microradians so that the geometrical errors associated with the translation of the movable mirror can be detected and further reduced. The drawback of the presented system is the overall sensitivity to long-term temperature drifts and relatively complicated manufacturing process.

A natural road further is the characterization of the system with the modifications proposed in previous sections, and then a practical evaluation of the closed-loop tilt compensation. It might also be interesting to push the tilt-detection further with more than four "pixels" [41]. Regarding the cyclic error, further experimentation and enhancement (mentioned before) would be also needed to investigate and push the limits.

Despite the recognized obstacles to be overcome, the presented system represents a way to easier adoption of the laser interferometry into dimensional optical metrology systems with the typical error sources in mind, leading to more straightforward integration together with smaller and well-defined measurement uncertainties.

Declaration of Competing Interest

The authors declare that they have no known competing financial interests or personal relationships that could have appeared to influence the work reported in this paper.

CRediT authorship contribution statement

Šimon Řeřucha: Conceptualization, Investigation, Methodology, Software, Validation, Data curation, Visualization, Writing - original draft, Writing - review & editing. **Miroslava Holá:** Investigation, Resources, Writing - review & editing. **Martin Šarbort:** Formal analysis, Writing - review & editing. **Jan Hrabina:** Methodology, Writing - review & editing. **Jindřich Oulehla:** Resources, Writing - review & editing. **Ondřej Číp:** Conceptualization, Supervision, Writing - review & editing. **Josef Lazar:** Conceptualization, Supervision, Writing - review & editing.

Acknowledgements

This EMPIR 17IND03 LaVA project has received funding from the EMPIR programme co-financed by the Participating States and from the European Union's Horizon 2020 research and innovation programme.

Authors acknowledge support from: the EMPIR programme (17IND03 LaVA); the Ministry of Industry and Trade of the Czech Republic (FV10336); the Technology Agency of the Czech Republic (TE01020233;TN01000008); the European Commission and the Ministry of Education, Youth and Sports of the Czech Republic (CZ.1.05/2.1.00/01.0017, LO1212, CZ.02.1.01/0.0/0.0/16_026/0008460); the Czech Academy of Sciences (RVO:68081731).

Supplementary material

Supplementary material associated with this article can be found, in the online version, at doi:10.1016/j.optlaseng.2021.106568 .

References

[1] Yang S, Zhang G. A review of interferometry for geometric measurement. Meas Sci Technol 2018;29:102001. doi:10.1088/1361-6501/aad732.
[2] Watchi J, Cooper S, Ding B, Mow-Lowry CM, Collette C. Contributed review: a review of compact interferometers. Rev Sci Instrum 2018;89:121501. doi:10.1063/1.5052042.
[3] Coveney T. A review of state-of-the-art 1D length scale calibration instruments. Meas Sci Technol 2020;31:042002. doi:10.1088/1361-6501/ab5f71.
[4] Bobroff N. Recent advances in displacement measuring interferometry. Meas Sci Technol 1993;4:907–26. doi:10.1088/0957-0233/4/9/001.
[5] Haitjema H. Calibration of displacement laser interferometer systems for industrial metrology. Sensors 2019;19. doi:10.3390/s19194100.
[6] Cip O, Petru F. A scale-linearization method for precise laser interferometry. Meas Sci Technol 2000;11:133–41. doi:10.1088/0957-0233/11/2/305.
[7] Ahn J, Kim J-A, Kang C, Kim J-W, Kim S. A passive method to compensate nonlinearity in a homodyne interferometer. Opt Express 2009;17:23299–308. doi:10.1364/OE.17.023299.
[8] Pozar T, Mozina J. Enhanced ellipse fitting in a two-detector homodyne quadrature laser interferometer. Meas Sci Technol 2011;22. doi:10.1088/0957-0233/22/8/085301.
[9] Kning R, Wimmer G, Witkovský V. Ellipse fitting by nonlinear constraints to demodulate quadrature homodyne interferometer signals and to determine the statistical uncertainty of the interferometric phase. Meas Sci Technol 2014;25:115001. doi:10.1088/0957-0233/25/11/115001.
[10] Birch KP, Downs MJ. An updated Edlén equation for the refractive index of air. Metrologia 1993;30:155–62. doi:10.1088/0026-1394/30/3/004.
[11] Birch KP, Downs MJ. Erratum: correction to the updated Edlén equation for the refractive index of air (Metrologia (1994) 31 (315–316)). Metrologia 1994;31:315–16. doi:10.1088/0026-1394/31/4/006.
[12] Ciddor PE. Refractive index of air: new equations for the visible and near infrared. Appl Opt 1996;35:1566–73. doi:10.1364/AO.35.001566.
[13] Hucl V, Cizek M, Hrabina J, Mikel B, Rerucha S, Buchta Z, Jedlicka P, Lesundak A, Oulehla J, Mrna L, Sarbort M, Smid R, Lazar J, Cip O. Automatic unit for measuring refractive index of air based on Ciddor equation and its verification using direct interferometric measurement method. Proc SPIE, vol 8788; 2013. doi:101117/122020756.
[14] Lazar J, Holá M, Číp O, Hrabina J, Oulehla J. Interferometric system with tracking refractometry capability in the measuring axis. Meas Sci Technol 2013;24:067001. doi:10.1088/0957-0233/24/6/067001.
[15] Flugge J, Weichert C, Hu H, Koning R, Bosse H, Wiegmann A, Schulz M, Elster C, Geckeler RD. Interferometry at the PTB nanometer comparator - design, status and development. In: Proc SPIE, vol. 7133; 2009. DOI: 10.1117/12.821252
[16] Weichert C, Quabis S, Flgge J. A new vacuum setup for fundamental investigations on interferometric length measurements. In: euspen's 18th international conference & exhibition, Venice, IT; 2018.

[17] Eves BJ. Design of a large measurement-volume metrological atomic force microscope (AFM). Meas Sci Technol 2009;20:084003. doi:10.1088/0957-0233/20/8/084003.
[18] Ducourtieux S, Poyet B. Development of a metrological atomic force microscope with minimized Abbe error and differential interferometer-based real-time position control. Meas Sci Technol 2011;22:094010. doi:10.1088/0957-0233/22/9/094010.
[19] Lazar J, Hrabina J, Šerý M, Klapetek P, Číp O. Multiaxis interferometric displacement measurement for local probe microscopy. Cent Eur J Phys 2012;10:225–31. doi:10.2478/s11534-011-0093-5.
[20] Weichert C, Köchert P, Köning R, Flügge J, Andreas B, Kuetgens U, Yacoot A. A heterodyne interferometer with periodic nonlinearities smaller than ±10 pm. Meas Sci Technol 2012;23:094005.
[21] Křen P, Balling P. Common path two-wavelength homodyne counting interferometer development. Meas Sci Technol 2009;20:084009. doi:10.1088/0957-0233/20/8/084009.
[22] Pisani M, Yacoot A, et al. Comparison of the performance of the next generation of optical interferometers. Metrologia 2012;49:455.
[23] Kramar JA, Dixson R, Orji NG. Scanning probe microscope dimensional metrology at NIST. Meas Sci Technol 2010;22:024001. doi:10.1088/0957-0233/22/2/024001.
[24] Schnenberger C, Alvarado SF. A differential interferometer for force microscopy. Rev Sci Instrum 1989;60:3131–4. doi:10.1063/1.1140543.
[25] Cunningham MJ, Cheng ST, Clegg WW. A differential interferometer for scanning force microscopy. Meas Sci Technol 1994;5:1350–4. doi:10.1088/0957-0233/5/11/005.
[26] Stone J. Test and calibration of displacement measuring interferometers. In: Proceedings of the 3rd international conference on mechanical metrology (CIMMEC III), Gramado, Brazil.; 2014.
[27] Downs MJ. A proposed design for an optical interferometer with sub-nanometric resolution. Nanotechnology 1990;1:27–30. doi:10.1088/0957-4484/1/1/005.
[28] Yacoot A, Downs MJ. The use of x-ray interferometry to investigate the linearity of the NPL differential plane mirror optical interferometer. Meas Sci Technol 2000;11:1126–30. doi:10.1088/0957-0233/11/8/305.
[29] Lazar J, Klapetek P, Číp O, Čížek M, Šerý M. Local probe microscopy with interferometric monitoring of the stage nanopositioning. Meas Sci Technol 2009;20:084007. doi:10.1088/0957-0233/20/8/084007.
[30] Lazar J, Klapetek P, Valtr M, Hrabina J, Buchta Z, Cip O, Cizek M, Oulehla J, Sery M. Short-range six-axis interferometer controlled positioning for scanning probe microscopy. Sensors 2014;14:877–86. doi:10.3390/s140100877.
[31] Guo D, Wang M. Self-mixing interferometry based on sinusoidal phase modulation and integrating-bucket method. Opt Commun 2010;283:2186–92. doi:10.1016/j.optcom.2010.01.025.
[32] Strube S, Molnar G, Danzebrink H. Compact field programmable gate array (FPGA)-based multi-axial interferometer for simultaneous tilt and distance measurement in the sub-nanometre range. Meas Sci Technol 2011;22. doi:10.1088/0957-0233/22/9/094026.
[33] Ducourtieux S, Ahamed D, Delvallee A. Minimization of Abbe error on the LNE's metrological AFM by alignment of interferometer laser beams using a CCD camera. Nanoscale 2019; 2019. DOI: 10.13140/RG.2.2.18895.43684
[34] Kning R, Flgge J, Bosse H. A method for the in-situ determination of Abbe errors and their correction. Meas Sci Technol 2007;18:476–81. doi:10.1088/0957-0233/18/2/s21.
[35] Rerucha S, Buchta Z, Sarbort M, Lazar J, Cip O. Detection of interference phase by digital computation of quadrature signals in homodyne laser interferometry. Sensors 2012;12:14095–112. doi:10.3390/s121014095. DOI: 10.3390/s121014095
[36] Rerucha S, Yacoot A, Pham TM, Cizek M, Hucl V, Lazar J, et al. Laser source for dimensional metrology: investigation of an iodine stabilized system based on narrow linewidth 633 nm DBR diode. Meas Sci Technol 2017;28. doi:10.1088/1361-6501/aa5ab9.
[37] Yacoot A, Kuetgens U. Sub-atomic dimensional metrology: developments in the control of x-ray interferometers. Meas Sci Technol 2012;23:074003. doi:10.1088/0957-0233/23/7/074003.
[38] Rerucha S, Mikel B, Matej Z, Herman O, Hola M, Jelinek M, Jedlicka P, Cip O, Lazar J. Linearized and compensated interferometric system for high-velocity traceable length calibration on a metre scale. In: Proc. SPIE, vol. 10976; 2018. DOI: 10.1117/12.2519461
[39] Leirset E, Engan HE, Aksnes A. Heterodyne interferometer for absolute amplitude vibration measurements with femtometer sensitivity. Opt Express 2013;21:19900–21. Http://www.opticsexpress.org/abstract.cfm?URI=oe-21-17-19900, 10.1364/OE.21.019900
[40] Leviton DB, Frey BJ. Temperature-dependent absolute refractive index measurements of synthetic fused silica. Optomechanical technologies for astronomy, vol 6273; 2006. 62732K. DOI: 10.1117/12.672853
[41] Sarbort M, Rerucha S, Jedlicka P, Lazar J, Cip O. Tilt angle measurement with a Gaussian-shaped laser beam tracking. In: Proc. SPIE, vol. 9132; 2014. DOI: 10.1117/12.2052880